3D full coupling model for strong interaction between a pulsating bubble and a movable sphere

Shuai Li[1], A-Man Zhang[1,†], Rui Han[1], Qingwei Ma[2]

[1]College of Shipbuilding Engineering, Harbin Engineering University, 145 Nantong Street, Harbin 150001, China

[2]School of Mathematics, Computer Science and Engineering, City University of London, United Kingdom

In this study, we establish a full coupling model (FCM) to simulate strong bubble-sphere interaction based on a three-dimensional boundary integral method. Different from the traditional loose coupling model (LCM), FCM adopts several auxiliary functions to deal with the mutual dependence between the hydrodynamic force and the sphere acceleration. In addition, the weighted moving least square method, a mesh density control scheme and an adaptive mesh refinement scheme are implemented to improve the quality of mesh on the deformable bubble surface. To validate the present model, convergence tests on different mesh sizes and time steps are conducted at first. The numerical results are also compared with the axisymmetric model, in which consistent results have been achieved. We further make comparisons between the numerical results and those from several experiments under different boundary conditions. For weak interaction cases, both LCM and FCM can give the results that have good agreement with the experiment data. As the interaction effects become stronger, the advantage of the FCM over the LCM becomes increasingly obvious. Particularly, when the pulsating bubble is in contact with the sphere surface, the essential physical features of the experiments can be well reproduced by the FCM while the predictions by the LCM are significantly different from the experiment. The present 3D model can be further extended to study more complex underwater contact explosions, cavitation inception on a structure and airgun bubble dynamics.

Keywords: bubble dynamics, sphere, full coupling model, boundary integral method

† Email address for correspondence: zhangaman@hrbeu.edu.cn

1. Introduction

Bubbles exist widely in nature and are crucial in fluid mechanics. Bubble dynamics is a focus for its important applications in many engineering fields. The bubbles undergo a violent oscillation when they are in a field of an imbalance pressure between the bubble gas and the ambient flow field. For an underwater explosion bubble [1-3] or an air-gun bubble [4, 5], violent expansion occurs at the very early stage since the gas pressure inside the bubble is much higher than the ambient hydrostatic pressure, which is followed by the bubble collapse as the gas pressure drops far below the ambient pressure. In hydraulic machinery field [6, 7], when a micro-bubble suffers from a sudden pressure drop due to high velocities in the flow, the bubble would expand explosively and collapse violently as the ambient pressure surrounding the bubble returns to a high value. Shock wave emission and high-speed liquid jet impact are often observed during the final stage of the bubble collapse [8], which are believed to be main factors responsible for cavitation erosion and devastating damages on vessels caused by underwater explosion bubbles. In addition, bubbles are very useful tools in ultrasonic cleaning[9, 10], shock wave lithotripsy [11], sonoporation [12], etc.

In the past several decades, the Boundary Integral Method (BIM) based on the potential flow theory has become one of the most successful numerical methods in bubble dynamic studies. It is well known that the BIM reduces the dimension of the problem by one, thus a much higher efficiency can be achieved. For a typical pulsating underwater explosion bubble, the Reynolds numbers are of the order of $O(10^8)$ [1, 13]. As such, the viscosity of the liquid hardly plays a role during the transient bubble motion. Additionally, the associated Mach number is larger than 0.1 only for about 0.1% of the bubble lifetime. Therefore, the assumptions of the BIM (the fluid surrounding the bubble inviscid and incompressible) stand well at least for the first cycle of an underwater explosion bubble. The BIM is also suitable for simulations of air-gun bubbles [14], cavitation bubbles [15, 16] and acoustic bubbles [17, 18].

Both axisymmetric [19-21] and three-dimensional [22-24] BIM models are found in the literature and a variety of physical phenomena associated with bubbles and cavitation have been studied. If the size of a submerged structure is much larger than the bubble, the structure is often simplified as a rigid plane structure. Then the image method [25, 26] can be adopted and there is no need to mesh the structure surface in computations. Otherwise, the structure boundary needs to be meshed with the zero flux condition imposed on it [27]. However, for a movable or deformable structure, the fast bubble pulsation and the

violent liquid jet impact may cause the movement of the structure. Thus, the boundary conditions for the flow domain are constantly changing and the bubble dynamic behaviors are affected accordingly. Harris[28] established a 3D numerical model to simulate the interaction between a bubble and a nearby movable structure. Thereafter, many numerical studies were conducted on bubble-structure interaction based on the loose coupling model (LCM) [2, 29-31].

This study focuses on the 3D transient bubble-sphere interaction problem, which is the most fundamental problem in bubble-structure interactions and still closely associated with applications to cavitation in silt-laden flow, ultrasonic cleaning and underwater explosion. It has been demonstrated that the rigid body motion of a sphere greatly affects the bubble motion while its high frequency local deformation has little effect [32]. Thus the sphere deformation is ignored in the present study. The present numerical model differs from those in published papers in, but not limited to, the following three aspects.

Firstly, in the framework of potential flow theory, the pressure is calculated by the unsteady Bernoulli equation and the force is obtained by integrating the pressure over the wetted surface of the structure. The main difficulty lies in the treatment of the φ_t term (the partial derivative of the potential with respect to time) in Bernoulli equation. In the LCM, the finite difference approximation is often adopted to calculate φ_t [1, 33, 34]. However, since the structure is movable, the result obtained by the finite difference is the material derivative rather than the partial derivative. The LCM gives reasonable results only if the structure response (velocity) is relatively small [2, 29, 35]. Besides, the small time step for a violently oscillating bubble leads to numerical instabilities in the LCM. To solve the problem of calculating the φ_t term, we incorporate the auxiliary function method [36] in 3D BIM to establish a full coupling model (FCM) that can well deal with the mutual dependence between the force and the sphere motion. The sphere acceleration can be accurately estimated by only using the quantities in the current time step without inner iteration. Compared with the traditional LCM, the FCM has a complete theoretical basis as well as excellent performance in numerical simulations.

Secondly, the singularity appears when the bubble surface and structure surface approach too close to each other, resulting in strong numerical instabilities. The traditional treatment is to control the distance between the bubble-nodes and structure-nodes no less than the mesh size [27, 31]. Another robust treatment is to remove the thin water layer between the bubble and the structure, and then join the remaining bubble surface and the structure surface together. However, this algorithm has only been

applied so far to axisymmetric model [36, 37]. In this study, we propose a 3D model for the interaction between a sphere and a nearly-hemispherical bubble that is attached to the sphere surface, which is reckoned as the key physical process to reveal the promotion mechanism of erosion in silt-laden flow [38-41]. Besides, the present 3D model can be further extended to study more complex phenomena involved in underwater contact explosions, and the interaction between airgun-body and attached airgun-bubbles.

Thirdly, the pressure and velocity fields in the flow are very useful to reveal the underlying mechanisms of bubble dynamic behaviors and the associated physical phenomena. Once the velocity potentials are given on the flow boundaries, the pressure and velocity fields can be calculated by the indirect boundary integral method (IBIM) [23, 42]. There are some studies on the pressure field with the axisymmetric model [42]. In this study, the pressure and velocity fields in 3D cases will be given.

To verify our numerical model, convergence studies on different mesh sizes and time steps are conducted at first. Then we compare the present 3D model with the axisymmetric model. In addition, several experiments are carried out for an underwater discharge bubble interacting with a suspended sphere under different boundary conditions. The present 3D model reproduces the experimental observations extremely well, including bubble dynamic behaviors and sphere motions. In particular, when the bubble is attached on the sphere surface, physical features including the bubble wrapping the sphere, the bubble necking and the mushroom shaped bubble at the final collapse stage are well simulated.

This paper is organized as follows. In Sec. 2, a discourse of the physical problem is given, together with introducing the essential parameters and the non-dimensionalization system. In Sec. 3, we establish a full coupling model of bubble-sphere interaction based on the 3D boundary integral method and propose some improved numerical techniques. In Sec. 4, convergence studies are conducted and comparisons are made between the 3D model and axisymmetric model. In Sec. 5, comparisons are made between the FCM and LCM in terms of accuracy. Sec. 6 shows comparisons between the numerical results and several experimental results under various boundary conditions. In Sec. 7, the key conclusions are made.

2. Physical problem and nondimensionalization

Consider the bubble-sphere interaction in three-dimensional configuration, as shown in Fig. 1. A Cartesian coordinate system *O-xyz* is defined, with the origin at the initial bubble center and *z* axis pointing upwards (the opposite direction of gravity). The bubble is assumed to be an initially tiny high-pressure spherical bubble. The bubble center is located at a distance *h* below the initially quiescent free surface and at a distance d_w from a vertical rigid wall. The coordinate of the initial sphere center is denoted by (x_0, y_0, z_0). The sphere mass is denoted by *M* and the radius by R_s.

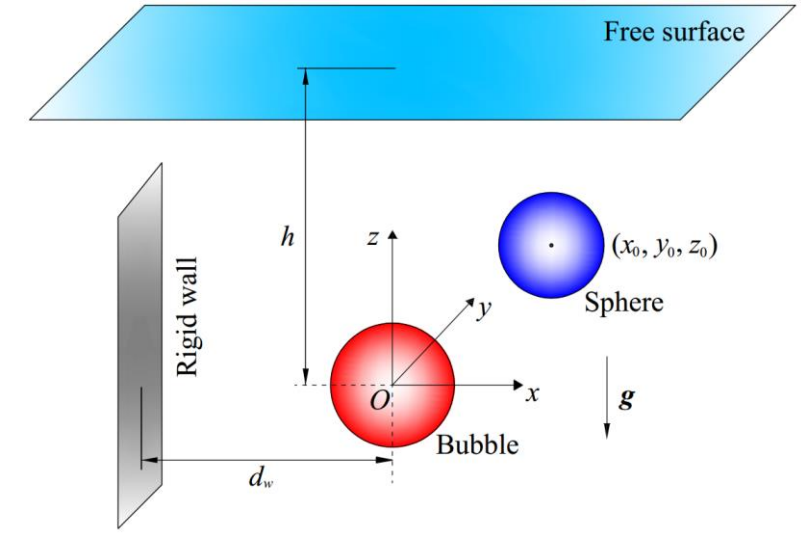

Fig. 1. Sketch and coordinate system for three-dimensional bubble-sphere interaction under various boundary conditions.

All physical quantities in the present study are defined in dimensionless form. A commonly used non-dimensionalization system is adopted as follows. The maximum equivalent bubble radius R_m is taken as the length scale, the liquid density ρ as the density scale and the hydrostatic pressure at the level of the initial bubble center $p_\infty = p_{atm} + \rho g h$ as the pressure scale (p_{atm} is the constant at the free surface, g is the gravity acceleration). All other quantities can be scaled with the above three fundamental quantities. For example, the velocity, acceleration and time are scaled by $\sqrt{p_\infty/\rho}$, $p_\infty/\rho R_m$ and $R_m\sqrt{\rho/p_\infty}$, respectively. The initial dimensionless geometrical parameters are defined as follows:

$$\gamma_w = d_w/R_m, \quad \gamma_f = h/R_m, \quad \lambda_L = R_s/R_m, \quad \lambda_\rho = 3M/\left(4\pi\rho R_s^3\right) \tag{1}$$

where λ_L and λ_ρ are the sphere-bubble size ratio and the sphere-liquid density ratio, respectively.

The initial dimensionless bubble radius and pressure in it are given as follows:

$$\overset{+}{R}_0 = R_0/R_m, \quad \varepsilon = p_0/p_\infty, \tag{2}$$

The initial dimensionless sphere center is denoted by $(\bar{x}_0, \bar{y}_0, \bar{z}_0)$, the dimensionless sphere mass is denoted by $\bar{M}$.

3. Numerical model

In the potential flow theory, the liquid is assumed incompressible and inviscid, and the liquid flow irrotational. These assumptions stand well in such transient physical problem associated with oscillating bubbles, at least for the first cycle of the bubble oscillation [19, 22, 23, 29, 43, 44]. In this section, we give a brief discourse of the standard 3D BIM. Then, the auxiliary function method is incorporated in the 3D BIM to establish a full coupling model. After that, the indirect boundary integral method is introduced to calculate the pressure and velocity fields. At last, some improved mesh optimization techniques are proposed.

3.1 Boundary Integral Method for bubble dynamics

Following the standard 3D BIM [22, 45], the velocity potential φ that satisfies the Laplace equation and the boundary integral equation is given as follows:

$$\nabla^2\varphi = 0, \tag{3}$$

$$c(\boldsymbol{r})\varphi(\boldsymbol{r}) = \iint_S \left[\frac{\partial\varphi(\boldsymbol{q})}{\partial n} G(\boldsymbol{r},\boldsymbol{q}) - \varphi(\boldsymbol{q}) \frac{\partial G(\boldsymbol{r},\boldsymbol{q})}{\partial n} \right] \mathrm{d}S, \tag{4}$$

where $\boldsymbol{r}$ and $\boldsymbol{q}$ are the control point and source point, respectively; S is the flow boundary; c is the solid angle; G is the Green function and $\boldsymbol{n}$ is the outward normal of S.

The kinematic boundary conditions on the bubble surface (S_b) and the free surface (S_f) are given by:

$$\frac{\mathrm{d}x}{\mathrm{d}t} = \frac{\partial\varphi}{\partial x}, \quad \frac{\mathrm{d}y}{\mathrm{d}t} = \frac{\partial\varphi}{\partial y}, \quad \frac{\mathrm{d}z}{\mathrm{d}t} = \frac{\partial\varphi}{\partial z}. \tag{5}$$

The dynamic boundary conditions on S_b and S_f are given by:

$$\frac{\mathrm{d}\varphi}{\mathrm{d}t}=\frac{|\nabla\varphi|^2}{2}-p_b-\delta^2 z+1 \quad \text{on } S_b, \tag{6}$$

$$\frac{\mathrm{d}\varphi}{\mathrm{d}t}=\frac{|\nabla\varphi|^2}{2}-\delta^2\left(z-\gamma_f\right) \quad \text{on } S_f, \tag{7}$$

where p_b is the pressure on the bubble surface, δ is the buoyancy parameter defined as $\delta=\sqrt{\rho g R_m/p_\infty}$.

Without the viscous effect, the moment acting on the sphere keeps zero, so only the translations of the sphere is considered in this study. On the sphere surface (S_s), the Neumann boundary condition can be expressed as:

$$\frac{\partial\varphi}{\partial n}=\boldsymbol{U}\cdot\boldsymbol{n}=U_x\cdot n_x+U_y\cdot n_y+U_z\cdot n_z, \tag{8}$$

where $\boldsymbol{U}$ is the velocity of the sphere.

The pressure field inside the bubble is assumed homogeneous and the adiabatic law is adopted to describe the bubble gas pressure [1, 23, 26]:

$$p_b=\varepsilon\left(\frac{V_0}{V}\right)^{\kappa}, \tag{9}$$

where κ is the ratio of the specific heat for the gas, V_0 is the initial bubble volume, and V is the bubble volume.

3.2 Velocity computation scheme

We use planer triangular elements to mesh bubble and sphere surfaces. On each element, linear interpolations are adopted for the velocity potential and the normal velocity. The boundary integral equation (4) transforms into a matrix form [46]:

$$[\mathbf{G}]\cdot[\mathbf{\Psi}]=[\mathbf{H}]\cdot[\mathbf{\Phi}], \tag{10}$$

where [$\mathbf{\Psi}$] and [$\mathbf{\Phi}$] are the column vectors of the normal velocity and the velocity potential on boundaries, respectively, and [**G**] and [**H**] are two matrices of influence coefficients.

Firstly, we consider a simple situation, i.e., the bubble is not attached to the sphere surface. At each time step, [$\mathbf{\Phi}$] on the bubble surface and [$\mathbf{\Psi}$] on the sphere surface are known. The known terms are moved to the right side and the unknown terms are moved to the left side to make the equations

solvable.

In this study, we further consider an interesting and challenging situation, i.e., the bubble is attached to the sphere surface, which is referred to as 'attached case' in the following discussion. The bubble surface and the sphere surface are joined together. Special attention must be paid to the bubble-sphere intersection line because the normal may not be continuous. Besides, the bubble and the sphere boundary conditions must be imposed simultaneously on this intersection line when calculating the velocity. Both the velocity potential and the normal velocity (as part of the sphere surface) on this intersection line are known, thus the number of the equations exceeds that of the unknowns. Liu et al.[47] adopted a double-node technique to solve this overdetermined problem in axisymmetric configuration with a fixed structure. This method is extended to 3D configurations with a movable structure in the present work. Each node on the intersection line is split into two nodes. The first one belongs to the bubble surface and the other one belongs to the sphere surface. Equation (10) transforms into:

$$\begin{bmatrix} \mathbf{G}_{bb} & \mathbf{G}_{bb_i} & \mathbf{G}_{bs_i} & \mathbf{G}_{bs} \\ \mathbf{G}_{b_ib} & \mathbf{G}_{b_ib_i} & \mathbf{G}_{b_is_i} & \mathbf{G}_{b_is} \\ \mathbf{G}_{s_ib} & \mathbf{G}_{s_ib_i} & \mathbf{G}_{s_is_i} & \mathbf{G}_{s_is} \\ \mathbf{G}_{sb} & \mathbf{G}_{sb_i} & \mathbf{G}_{ss_i} & \mathbf{G}_{ss} \end{bmatrix} \cdot \begin{bmatrix} \boldsymbol{\Psi}_b \\ \boldsymbol{\Psi}_{b_i} \\ \boldsymbol{\Psi}_{s_i} \\ \boldsymbol{\Psi}_s \end{bmatrix} = \begin{bmatrix} \mathbf{H}_{bb} & \mathbf{H}_{bb_i} & \mathbf{H}_{bs_i} & \mathbf{H}_{bs} \\ \mathbf{H}_{b_ib} & \mathbf{H}_{b_ib_i} & \mathbf{H}_{b_is_i} & \mathbf{H}_{b_is} \\ \mathbf{H}_{s_ib} & \mathbf{H}_{s_ib_i} & \mathbf{H}_{s_is_i} & \mathbf{H}_{s_is} \\ \mathbf{H}_{sb} & \mathbf{H}_{sb_i} & \mathbf{H}_{ss_i} & \mathbf{H}_{ss} \end{bmatrix} \cdot \begin{bmatrix} \boldsymbol{\Phi}_b \\ \boldsymbol{\Phi}_{b_i} \\ \boldsymbol{\Phi}_{s_i} \\ \boldsymbol{\Phi}_s \end{bmatrix}, \tag{11}$$

where the subscripts b and s denote the nodes that belong to the bubble surface and sphere surface, respectively, the subscripts b_i and s_i denote the nodes on the intersection line that belongs to the bubble surface and sphere surface, respectively. Considering nodes b_i and s_i share the same coordinates and $\boldsymbol{\Phi}_{b_i} = \boldsymbol{\Phi}_{s_i}$, Equation (11) transforms into:

$$\begin{bmatrix} \mathbf{G}_{bb} & \mathbf{G}_{bb_i} & -\mathbf{H}_{bs} \\ \mathbf{G}_{b_ib} & \mathbf{G}_{b_ib_i} & -\mathbf{H}_{b_is} \\ \mathbf{G}_{sb} & \mathbf{G}_{sb_i} & -\mathbf{H}_{ss} \end{bmatrix} \cdot \begin{bmatrix} \boldsymbol{\Psi}_b \\ \boldsymbol{\Psi}_{b_i} \\ \boldsymbol{\Phi}_s \end{bmatrix} = \begin{bmatrix} \mathbf{H}_{bb} & \mathbf{H}_{bb_i} + \mathbf{H}_{bs_i} & -\mathbf{G}_{bs_i} & -\mathbf{G}_{bs} \\ \mathbf{H}_{b_ib} & \mathbf{H}_{b_ib_i} + \mathbf{H}_{b_is_i} & -\mathbf{G}_{b_is_i} & -\mathbf{G}_{b_is} \\ \mathbf{H}_{sb} & \mathbf{H}_{sb_i} + \mathbf{H}_{ss_i} & -\mathbf{G}_{ss_i} & -\mathbf{G}_{ss} \end{bmatrix} \cdot \begin{bmatrix} \boldsymbol{\Phi}_b \\ \boldsymbol{\Phi}_{b_i} \\ \boldsymbol{\Psi}_{s_i} \\ \boldsymbol{\Psi}_s \end{bmatrix}. \tag{12}$$

All the known terms have been moved to the right side, thus the unknown terms on the left side can be solved. The tangential velocity can be obtained by a finite difference scheme and the material velocity of nodes b and s can be obtained afterwards [22]. As for a node k on the intersection line, the following 3×3 matrix equation is used to compute the material velocity:

$$\begin{bmatrix} \boldsymbol{n}_k^b \\ \boldsymbol{n}_k^s \\ \boldsymbol{r}_k - \boldsymbol{r}_{k'} \end{bmatrix} \cdot \nabla \varphi_k = \begin{bmatrix} \Psi_b \\ \Psi_s \\ \varphi_k - \varphi_{k'} \end{bmatrix}, \tag{13}$$

where $\boldsymbol{n}_k^b$ and $\boldsymbol{n}_k^s$ are unit normal vectors on the bubble surface and sphere surface, respectively, k' is the neighboring node connected to node k on the intersection line.

3.3 Auxiliary function method for sphere motion

Firstly, we consider a simple situation where the bubble is not attached to the sphere surface. The kinematic equation for the sphere of three DOF is governed by Newton's second law:

$$[\mathbf{F}]_{3\times1} + [\mathbf{F}_e]_{3\times1} = [\mathbf{m}]_{3\times3} \cdot [\mathbf{a}]_{3\times1}, \tag{14}$$

where [**F**] is a column of hydrodynamic force, [$\mathbf{F}_e$] is a column of external force (e.g., the force due to gravity), $[\mathbf{m}] = diag(\bar{M}, \bar{M}, \bar{M})$ is the sphere mass matrix ($\bar{M} = M/\rho R_m^3$) and [**a**] is a column of sphere acceleration with three translations.

The hydrodynamic force $\boldsymbol{F}$ acting on the sphere can be obtained by integrating the pressure over its wetted surface S_s,

$$[\mathbf{F}] = [F_x, F_y, F_z] = -\iint_{S_s} (\varphi_t + \frac{1}{2}|\nabla\varphi|^2 + \delta^2 z - 1)\boldsymbol{n} \mathrm{d}S. \tag{15}$$

where the partial derivative of the potential with respect to time φ_t is unknown even if the velocity potentials on all boundaries of the flow domain are obtained. In the LCM, the backward finite difference approximation is often adopted to calculate φ_t [1, 33, 48]. However, since the sphere is movable in the present study, the material derivative ($\mathrm{d}\varphi/\mathrm{d}t$) rather than the partial derivative is obtained by the finite difference. In the following, the auxiliary function method is adopted to calculate the solution of φ_t.

The term φ_t also satisfies the Laplace equation in the flow [32]:

$$\nabla^2 \varphi_t = 0. \tag{16}$$

The boundary conditions of φ_t on the bubble surface (S_b), the free surface (S_f) and the sphere surface (S_s) are given by:

$$\varphi_t = 1 - \varepsilon\left(\frac{V_0}{V}\right)^{\kappa} - \frac{1}{2}\left|\nabla\varphi\right|^2 - \delta^2 z \qquad \text{on } S_b, \tag{17}$$

$$\varphi_t = -\frac{1}{2}\left|\nabla\varphi\right|^2 - \delta^2\left(z - \gamma_f\right) \qquad \text{on } S_f, \tag{18}$$

$$\frac{\partial\varphi_t}{\partial n} = \boldsymbol{a}\cdot\boldsymbol{n} - \boldsymbol{U}\cdot\frac{\partial\nabla\varphi}{\partial n} \qquad \text{on } S_s, \tag{19}$$

where φ_t on S_b and S_f can be easily obtained via Equations (17) and (18) once the velocity potentials of the flow domain are solved, however, the $\partial\varphi_t/\partial n$ term cannot be obtained through Equation (19) directly because the sphere acceleration is unknown. To handle this problem, we further introduce four auxiliary functions σ, ζ_x, ζ_y and ζ_z that satisfy Laplace equation, and φ_t can be written as:

$$\varphi_t = \sigma - \boldsymbol{U}\cdot\nabla\varphi + a_x\zeta_x + a_y\zeta_y + a_z\zeta_z. \tag{20}$$

The boundary conditions of σ, ζ_x, ζ_y and ζ_z can be written as:

$$\sigma = \boldsymbol{U}\cdot\nabla\varphi + 1 - \varepsilon\left(\frac{V_0}{V}\right)^{\kappa} - \frac{1}{2}\left|\nabla\varphi\right|^2 - \delta^2 z \qquad \text{on } S_b, \tag{21}$$

$$\sigma = \boldsymbol{U}\cdot\nabla\varphi - \frac{1}{2}\left|\nabla\varphi\right|^2 - \delta^2\left(z - \gamma_f\right) \qquad \text{on } S_f, \tag{22}$$

$$\frac{\partial\sigma}{\partial n} = 0 \qquad \text{on } S_s, \tag{23}$$

$$\zeta_x = 0, \quad \zeta_y = 0, \quad \zeta_z = 0 \qquad \text{on } S_b \text{ and } S_f, \tag{24}$$

$$\frac{\partial\zeta_x}{\partial n} = 0, \quad \frac{\partial\zeta_y}{\partial n} = 0, \quad \frac{\partial\zeta_y}{\partial n} = 0 \qquad \text{on } S_s. \tag{25}$$

The value of σ, ζ_x, ζ_y and ζ_z on the sphere surface can be calculated in a manner similar to that used for φ. Considering the sphere gravity, Equation (14) transforms into:

$$\left(\begin{bmatrix}\bar{M} & 0 & 0\\ 0 & \bar{M} & 0\\ 0 & 0 & \bar{M}\end{bmatrix} + \begin{bmatrix}N_{xx} & N_{xy} & N_{xz}\\ N_{yx} & N_{yy} & N_{yz}\\ N_{zx} & N_{zy} & N_{zz}\end{bmatrix}\right)\cdot\begin{bmatrix}a_x\\ a_y\\ a_z\end{bmatrix} = \begin{bmatrix}f_x\\ f_y\\ f_z\end{bmatrix} + \begin{bmatrix}0\\ 0\\ -\delta^2\bar{M}\end{bmatrix}, \tag{26}$$

where

$$N_{ij} = \iint_{S_s}\zeta_i\cdot n_j \mathrm{d}S, \tag{27}$$

$$f_i = -\iint_{S_s}(\sigma - \boldsymbol{U}\cdot\nabla\varphi + \frac{1}{2}\left|\nabla\varphi\right|^2 + \delta^2 z - 1)n_i \mathrm{d}S. \tag{28}$$

The sphere acceleration $\boldsymbol{a}$ can be solved directly via Equation (26) as all the other quantities have been obtained.

We further consider a more complex situation in which the bubble is attached to the sphere surface. The sphere surface S_s is divided into the wetted sphere surface S_{s1} and unwetted sphere surface S_{s2}. Both the hydrodynamic force and the gas dynamic force are included in the kinematic equation of the sphere. The bubble gas pressure acts on the unwetted sphere surface S_{s2} directly. The hydrodynamic force is calculated by the same method as given above. Equation (26) transforms into:

$$\left(\begin{bmatrix} \bar{M} & 0 & 0 \\ 0 & \bar{M} & 0 \\ 0 & 0 & \bar{M} \end{bmatrix} + \begin{bmatrix} N_{xx} & N_{xy} & N_{xz} \\ N_{yx} & N_{yy} & N_{yz} \\ N_{zx} & N_{zy} & N_{zz} \end{bmatrix}\right) \cdot \begin{bmatrix} a_x \\ a_y \\ a_z \end{bmatrix} = \begin{bmatrix} f_x \\ f_y \\ f_z \end{bmatrix} + \begin{bmatrix} 0 \\ 0 \\ -\delta^2 \bar{M} \end{bmatrix} + \begin{bmatrix} f_x^* \\ f_y^* \\ f_z^* \end{bmatrix}, \tag{29}$$

where

$$f_i^* = \iint_{S_{s2}} \varepsilon \left(\frac{V_0}{V}\right)^{\kappa} \cdot n_i \mathrm{d}S. \tag{30}$$

3.4 Pressure fields computation

It is well known that the BIM needs only the flow boundaries to be tracked. However, the pressure fields are very useful to reveal the underlying mechanisms of bubble dynamic behaviors. In this study, the pressure and velocity fields in 3D cases are calculated by the indirect boundary integral method (IBIM) [23, 42].

The concept of source density ω is introduced in IBIM, and the potential can be expressed as:

$$\varphi(\boldsymbol{r}) = \iint_S \omega(\boldsymbol{q}) \cdot G(\boldsymbol{r}, \boldsymbol{q}) \mathrm{d}S. \tag{31}$$

Firstly, the control points are placed on the bubble surface, thus Equation (31) transforms into a matrix form:

$$[\boldsymbol{\Phi}] = [\mathbf{G}] \cdot [\boldsymbol{\omega}], \tag{32}$$

where [**G**] is a matrix of influence coefficients that has been obtained when solving the boundary integral equation, [$\boldsymbol{\omega}$] is a column of source density, which can be obtained through $[\mathbf{G}]^{-1} \cdot [\boldsymbol{\Phi}]$. The velocity in the flow field can be calculated by inserting [$\boldsymbol{\omega}$] into the following Equation:

$$\nabla\varphi(\boldsymbol{r}) = \iint_S \omega(\boldsymbol{q}) \cdot \nabla G(\boldsymbol{r}, \boldsymbol{q}) \mathrm{d}S, \tag{33}$$

The same procedure applies to φ_t thus obtaining another source density. Then, the control points are placed in the flow field and the corresponding value of φ_t induced by all the sources can be

evaluated by the integration over the boundary surfaces. Substituting φ_t and the velocity term into the unsteady Bernoulli equation yields the pressure in the flow field.

3.5 Mesh optimization techniques

3.5.1 A weighted moving least-square smoother

Zhang et al.[22] proposed a smoothing scheme based on least square to eliminate the numerical instabilities of 3D toroidal bubbles. Wang [49] adopted a weighted moving least-square method to interpolate the free surface when modelling the ship waves. In this study, another weighted function is used, which has been proved accurate and robust.

Consider a single node (denoted by A) and its surrounding elements that need smoothing. A local Cartesian coordinate system, *O-XYZ*, is defined with its origin at the point A and the *Z* axis along the normal direction of the bubble surface at the node. A second order polynomial is employed for the bubble surface as follows,

$$Z = f(X,Y) = \alpha_1 X^2 + \alpha_2 XY + \alpha_3 Y^2 + \alpha_4 X + \alpha_5 Y + \alpha_6, \tag{34}$$

where $\alpha_1, \alpha_2 \cdots \alpha_6$ are coefficients that need to be determined by minimizing the following error function,

$$E(\alpha_1,\alpha_2,\alpha_3,\alpha_4,\alpha_5,\alpha_6) = \sum_{k=1}^{n_A} W_k [f(X_k,Y_k) - Z_k]^2, \tag{35}$$

where n_A is the number of the nodes that surround node A and W_k is a weighted function. The weighted function W_k is given by,

$$W_k = \begin{cases} \dfrac{2}{3} - 4\bar{s}^2 + 4\bar{s}^3 & (\bar{s} \le \dfrac{1}{2}) \\ \dfrac{4}{3} - 4\bar{s} + 4\bar{s}^2 - \dfrac{4}{3}\bar{s}^3 & (\dfrac{1}{2} < \bar{s} \le 1), \\ 0 & (\bar{s} > 1) \end{cases} \tag{36}$$

where $\bar{s} = \dfrac{s}{s_{max}}$ and $s = |\boldsymbol{r}_A - \boldsymbol{r}_k|$, s_{max} is the maximum distance from the surrounding nodes to node *A*.

Let $\dfrac{\partial E}{\partial \alpha_j} = 0$, yielding

$$\sum_{j=1}^{6} A_{ij}\alpha_j = B_i, (i = 1, 2, \ldots, 6), \tag{37}$$

where A_{ij} are B_i given as below

$$\left.\begin{aligned} &A_{ij} = \sum_{k=1}^{n_A} W_k \zeta_{kj} \zeta_{ki}, \qquad B_i = \sum_{k=1}^{n_A} W_k Z_k \zeta_{ki}, \\ &\zeta_{k1} = X_k^2, \zeta_{k2} = X_k Y_k, \zeta_{k3} = Y_k^2 \\ &\zeta_{k4} = X_k, \quad \zeta_{k5} = Y_k, \quad \zeta_{k6} = 1 \end{aligned}\right\} \quad (k = 1, 2, \ldots n_A). \tag{38}$$

After $\alpha_1, \alpha_2 \cdots \alpha_6$ are found, the smoothed coordinate of node A is (0, 0, α_6). The same procedure applies to the smoothing of the velocity potentials on the bubble surface.

3.5.2 A mesh density controller

In the BIM computation, nodes often overcrowd at some local positions, leading to a poor mesh quality. An elastic mesh technique (EMT) is put forward by Wang et al.[45] to handle this problem. Inspired by EMT, Zhang et al.[24, 50] proposed a more flexible method, i.e., density potential method (DPM). The DPM is used in the present study to control the mesh density (the node distribution) on both the bubble surface and the sphere surface. In the DPM, the node positions are updated in time with the true normal velocity $\boldsymbol{u}_n$ plus an artificial tangential velocity $\boldsymbol{u}_\tau$. The latter is the key to achieving a desired mesh quality, which is related to the density potential Θ introduced in the DPM. A uniform mesh is obtained if Θ is defined as a constant all over the bubble surface, otherwise nodes tend to gather to the location with a relatively large Θ. The DPM is a very powerful tool when simulating nonspherical bubbles because a finer mesh for the part of the bubble surface with large curvature can be easily obtained by the DPM. Here we give the form of Θ used in our numerical simulation, and the details of specifying the artificial tangential velocity $\boldsymbol{u}_\tau$ through Θ can be found in our previously published papers [24, 50].

Generally, we define the density potential Θ of node i as follows:

$$\Theta_i = \sum_{j=1}^{n_e} S_{i,j} \cdot \frac{1}{n_e} \cdot N(\varphi_i), \tag{39}$$

where n_e is the number of the elements connected to node i, $S_{i,j}$ is the area of the j^{th} element, N is a normalization operator. The curvature and velocity can also be incorporated in Equation (39) though it is not done in the present study.

When the DPM velocity $\boldsymbol{u}_D = \boldsymbol{u}_n + \boldsymbol{u}_\tau$ is used to update the bubble surface, the dynamic boundary

condition (6) is rewritten as follows:

$$\frac{\mathrm{d}\varphi}{\mathrm{d}t} = \nabla\varphi \cdot \boldsymbol{u}_D - \frac{|\nabla\varphi|^2}{2} + 1 - p_b - \delta^2 z, \tag{40}$$

In this study, the DPM technique is applied once every 3 time steps during the collapsing phase of the bubble.

3.5.3 Mesh topology treatment and refinement

If the bubble is not attached to the sphere surface, satisfactory results can be achieved by combining the mesh smoother and mesh density controller. However, for the challenging 'attached case', a high quality mesh of the bubble (sphere) surface is maintained by further implementing mesh topology treatment and refinement.

In 'attached cases', both large deformations of the bubble surface and large variations of the sphere wetted surface are observed, resulting in severely stretched and distorted elements. Given this, the edge swapping procedure is applied in our simulations based on a principle of maximizing the minimal angle of all corners of the elements that sharing one edge [24]. In addition, during the expansion phase of the bubble, the mesh size of the bubble surface increases when that of the sphere surface relatively decreases. The mismatch of the elements will lead to a decrease in both computational accuracy and efficiency, sometimes even causing an early breakdown of computation. Following Zhang et al. [22], the adaptive mesh refinement scheme is adopted to maintain a high quality mesh, which splits large elements and merges very small elements to prevent nonuniformity of element sizes from developing.

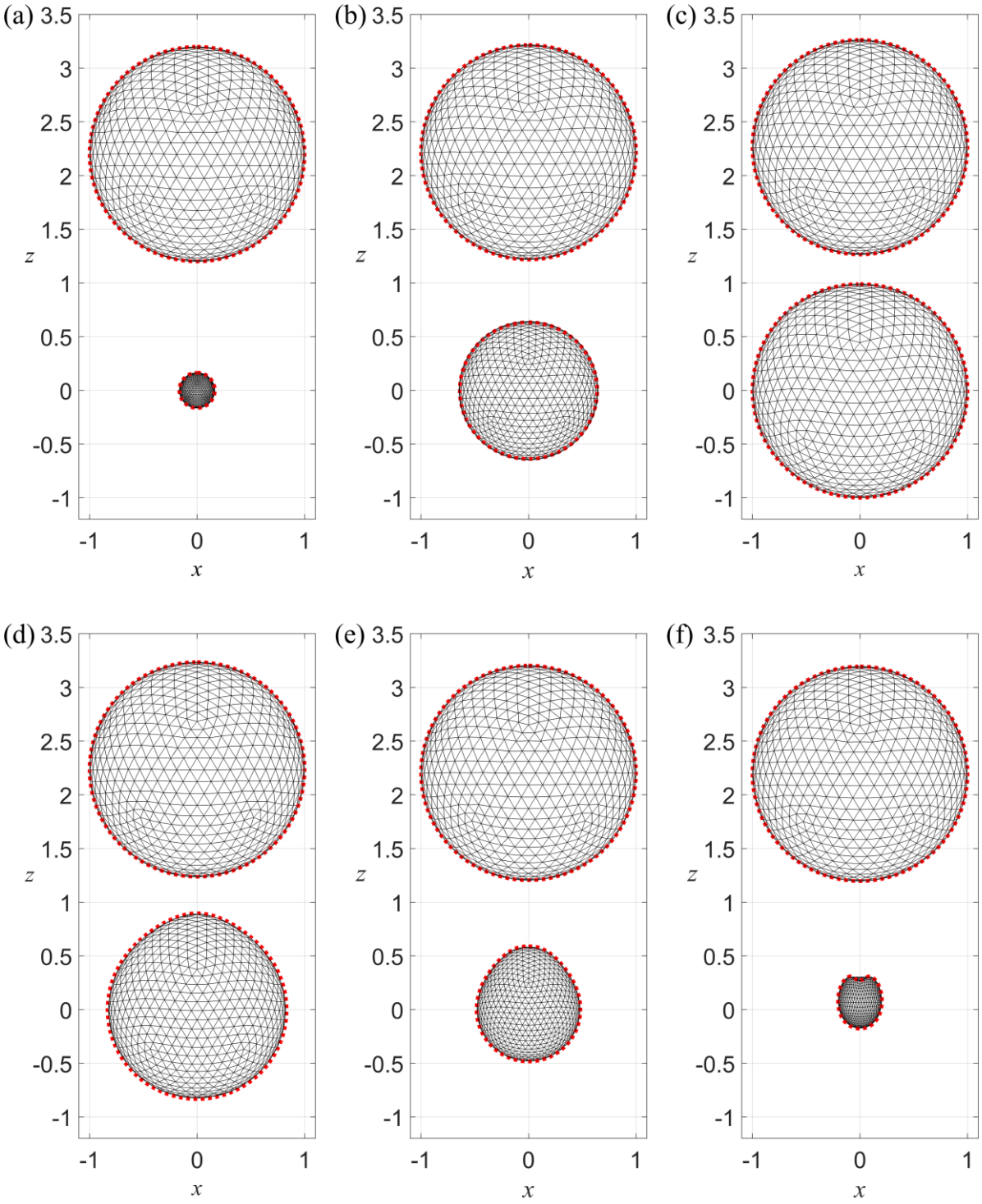

Fig. 2 Comparison of the bubble shapes (the lower ones) and sphere locations (the upper ones) between the present 3D model and the axisymmetric model (red dashed lines, Li et al. [36]) for $\lambda_L = 1$, $\lambda_\rho = 1$, $\left(\overline{x}_0, \overline{y}_0, \overline{z}_0\right) = (0, 0, 2.2)$, $\varepsilon = 100$ and $\kappa = 1.4$. The dimensionless times are 0, 0.203, 1.009, 1.539, 1.838 and 1.932, respectively.

4. Convergence study and comparison with the axisymmetric BIM model

In this section, we perform convergence tests of our 3D bubble-sphere interaction model at different element numbers of the bubble surface, N_e = 2000, 2880 and 5120, respectively. The number of elements on the sphere surface is fixed at 2000, which is adequate to achieve a convergent result. Meanwhile, the present 3D simulations are compared with the results obtained by the axisymmetric BIM model [36, 38], in which the sphere surface and bubble surface are meshed into 200 linear elements respectively. The dimensionless parameters are set as: $\lambda_L = 1$, $\lambda_\rho = 1$, $(\bar{x}_0, \bar{y}_0, \bar{z}_0) = (0, 0, 2.2)$, $\varepsilon = 100$ and $\kappa = 1.4$. Fig. 2 shows the comparison between the numerical results using 3D model (N_e = 2000) and axisymmetric model (denoted by red dashed lines) at typical time steps. In this case, the Green function in Equation (4) is taken as

$$G(\boldsymbol{r},\boldsymbol{q}) = \frac{1}{|\boldsymbol{r}-\boldsymbol{q}|}, \tag{41}$$

As shown in Fig. 2 (a~c), the bubble keeps a spherical shape during the expansion phase, and the sphere is pushed upward. During the collapsing phase, the motion of the bubble top is retarded by the presence of the sphere, leading to a relatively high curvature of the bubble top, as shown in Fig. 2 (d~e). During the final stage of the collapsing phase, a dent (the beginning of jet formation) is observed at the bubble top surface, while the bubble bottom still keeps a round shape, as shown in Fig. 2 (f). The underlying mechanism is given by Lauterborn [51], i.e., the highest-curvature region of the bubble surface collapses faster than other regions and is easier to trigger a jet, according to a proportional relationship between bubble radius and Rayleigh collapse time. The numerical results obtained by two models agree well with each other, in terms of bubble surface evolution and sphere motion. The relative error of the maximum sphere displacement between the present 3D model and the axisymmetric model is 0.12%, indicating the present 3D bubble-sphere interaction model has comparable accuracy with the axisymmetric model.

Fig. 3 shows the bubble shapes just before the jet impact with different N_e. Within a quite short time ($1.932 < t < 1.954$), a sharp upward liquid jet forms at the bubble bottom while the downward jet has a relatively larger width. The two axial jets collide in the middle of the bubble. With the mesh density controller, more nodes gather to the jet zone. As N_e increases (the mesh size decreases), the

results of the 3D model become identical and approach to the axisymmetric result (the relative error of the upward jet velocity at the impact moment decreases from 6.6% to 0.68%). N_e is chosen as 5120 in the following computations for accuracy.

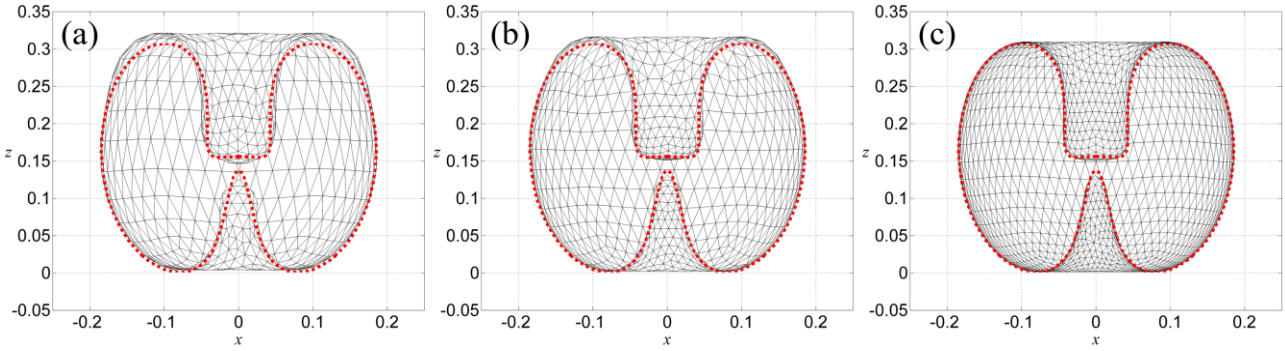

Fig. 3 The bubble shapes just before the jet impact $t = 1.954$ with different element numbers of the bubble surface for the same case in Fig. 2: (a) $N_e = 2000$, (b) $N_e = 2880$, and (c) $N_e = 5120$, compared to the axisymmetric model (red dashed line).

We further conduct convergence test with time step for the same case in Fig. 2. The time step is chosen as:

$$\Delta t = \frac{C_t}{\max\left|\left|\nabla\varphi\right|^2/2 + 1 + p_b + \delta^2 z\right|}, \tag{42}$$

where C_t is a constant.

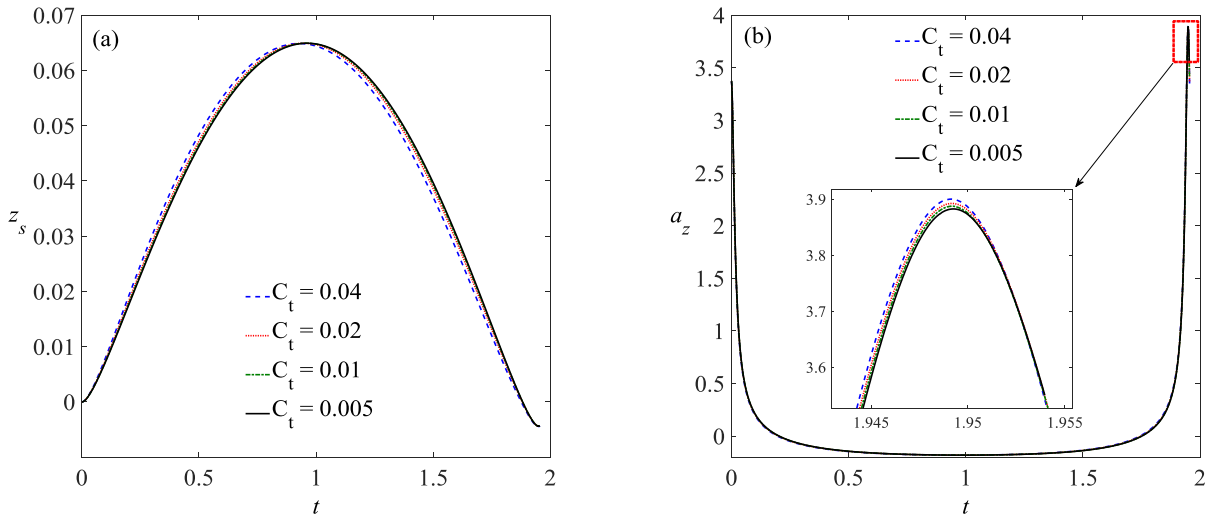

Fig. 4 Convergence test with time step for the same case in Fig. 2: (a) time histories of sphere displacements, (b) time histories of sphere accelerations.

We set C_t as 0.04, 0.02, 0.01 and 0.005, respectively. Fig. 4 shows some quantitative comparisons between the four cases. The time histories of sphere displacements are given in Fig.4 (a), which implies that the sphere is pushed upward by the expanding bubble and pulled downward by the collapsing bubble. The time histories of sphere accelerations are given in Fig. 4 (b). As C_t decreases from 0.04 to 0.005, the relative error of the maximum a_z decreases from 0.35% to 0.11%. It is worth noting that the sphere has a positive acceleration during the early expansion phase and the final collapsing phase, but the sphere acceleration is negative during most of the bubble life ($t>0.25$ and $t<0.7$). In both the figures, the results tend to coincide as C_t decreases and $C_t = 0.005$ is chosen in the following computations for studying accuracy and efficiency.

5. Comparison between LCM and FCM

In the present study, we propose the full coupling model (FCM) for a 3D bubble interacting with a movable body, in which the bubble motion and the body (sphere) acceleration are solved simultaneously as discussed in Section 3. However, the loose coupling model (LCM) is widely adopted in previous publications [1, 29, 31, 33, 35, 52], in which the output of the BIM is used as a loading condition for the structure and the structure solver provides a new boundary condition for the BIM. That is, the hydrodynamic force acting on the sphere is obtained via Equation (15), where the φ_t term is calculated explicitly using the backward difference method. The sphere acceleration is thus obtained by substituting the hydrodynamic force into Equation (14), and then the velocity and location of the sphere can be updated. Therefore, it is prudent to compare the above two methods in terms of accuracy.

Firstly, the LCM is used to simulate the same case in Fig. 2. N_e is chosen as 5120 and different time steps are adopted. Fig. 5 (a) shows the time histories of sphere displacements obtained by the LCM and the present FCM. There exists an visible discrepancy between the LCM and the FCM. Fig. 5 (b) shows the time histories of sphere accelerations. Numerical instabilities (high frequency oscillations) are observed in the results of the LCM, evidenced by the fact that the numerical oscillation becomes stronger as the time step (C_t) decreases, demonstrating that the convergence property of the LCM with time step is poor. On the contrary, the results obtained by the FCM stay stable without fluctuation during the whole bubble life, indicating the higher accuracy and better

stability of the FCM than that of the LCM.

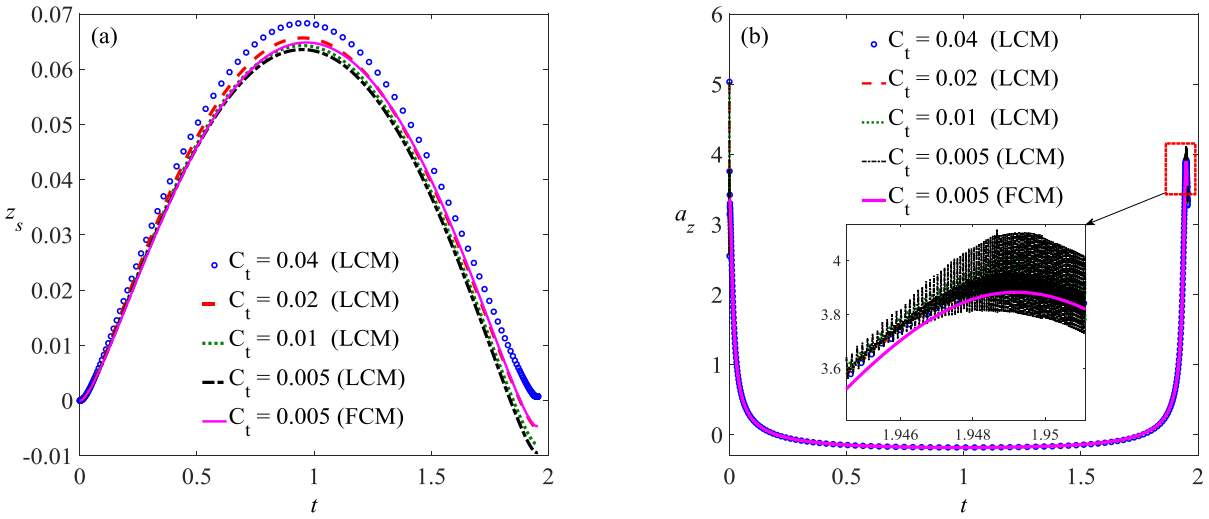

Fig. 5 Convergence tests of the traditional loose coupling model (LCM) with different time steps for the same case in Fig. 2, compared to the present full coupling model (FCM). (a) Time histories of sphere displacement. (b) Time histories of sphere acceleration.

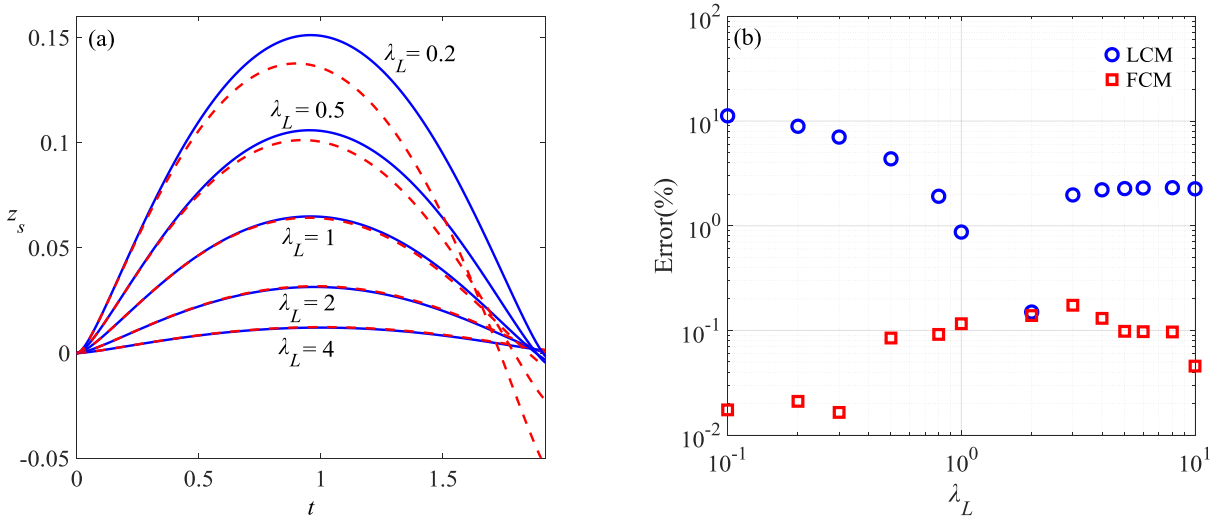

Fig. 6 (a) Comparisons of the sphere displacement between FCM (blue solid lines) and LCM (red dashed lines) with different size ratios λ_L. (b) The relative error of the maximum sphere displacement obtained by the LCM and FCM versus the size ratio.

It is also noted that the accuracy of the LCM can be greatly reduced in the following two situations. Firstly, with the increase of the sphere velocity and displacement as λ_L decreases, the accuracy of

backward difference method cannot be ensured, resulting in the inaccuracy of the hydrodynamic force. To study the situation in more details, several simulations are conducted with λ_L ranging from 0.1 to 10. Other parameters are set as: $\lambda_\rho = 1$, $(x_0, y_0, z_0) = (0, 0, 2.2)$, $\varepsilon = 100$, $\kappa = 1.4$, $N_e = 5120$ and $C_t = 0.005$. Fig. 6 (a) shows the comparison of time histories of the sphere displacement from the above two models. As expected, the discrepancy between the two models increases as λ_L decreases. The relative errors of the maximum sphere displacement obtained by the LCM and the FCM versus λ_L are plotted in Fig. 6 (b). As can be seen, the relative error of the FCM is always less than 0.2% while the relative error of the LCM increases rapidly as λ_L decreases below 1. For example, at λ_L =0.1, the relative error of the LCM can reach to 11%. On the other hand, when $\lambda_L > 1$, the relative error of LCM is only ~2%. This may be attributed to the fact that the sphere velocity increase as λ_L decreases and the effect of the fluid-structure interaction becomes stronger. Such effect is not well accounted for by the LCM.

Secondly, the accuracy of the LCM also decreases when the sphere-liquid density ratio λ_ρ is smaller than 1. In the extreme case, the LCM stops working when the sphere mass or λ_ρ approaches zero because Equation (14) has no solution. In the FCM, however, the sphere acceleration can be calculated through Equation (26) by taking the added mass into consideration.

6. Comparison between experimental and numerical results

6.1 Bubble-sphere interaction beneath a free surface

In this and the subsequent sections, comparisons will be made between the numerical results and experimental observations under different boundary conditions. The experiments are conducted in a 500×500×500 mm^3 water tank, and the bubbles are generated by the underwater electric discharge method. A high speed camera is used to capture the transient bubble-sphere interaction. More details about the experimental setup can be found in our previously published papers [36, 38].

The first experiment of bubble-sphere interaction is conducted beneath a free surface, in which the sphere diameter is 39.5mm, the sphere mass is 32.3g, the maximum equivalent bubble radius is about 18.7 mm, the minimum distance between the initial bubble center and the sphere surface is 18.7mm, and the water depths of the initial bubble center and the initial sphere center are both 41.2mm. According to the experimental data, the initial parameters in the numerical simulation are set as: λ_L =

1.06, $\lambda_\rho = 1$, $\left(\overline{x}_0, \overline{y}_0, \overline{z}_0\right)$ = (-2.05, 0, 0), $\gamma_f = 2.2$, $\varepsilon = 100$ and $\kappa = 1.4$. Since the bubble and sphere are located relatively far away from the free surface, the free surface almost keeps quiescent during the first period of the bubble. Following Klaseboer et al.[27], the flat free surface is modelled using a negative image of the bubble and the sphere to avoid the integrals over the free surface in the simulation. The Green function in Equation (4) is taken as:

$$G(\boldsymbol{r},\boldsymbol{q}) = \frac{1}{|\boldsymbol{r}-\boldsymbol{q}|} - \frac{1}{|\boldsymbol{r}-\boldsymbol{q}'|}, \tag{43}$$

where $\boldsymbol{q}'$ is the reflected image of $\boldsymbol{q}$ across the free surface.

Fig. 7 shows the comparison between the experimental images and numerical results during the first period of the bubble. The pressure and velocity fields are also provided for better elucidation of the underlying mechanisms. In Fig.7 (a), the bubble containing high pressure gas is generated at the initial time and the pressure is almost axisymmetrically distributed about the center line of the bubble-sphere system, except for a small region near the sphere surface. Apparently, the pressure acting on the right side of the sphere surface is slightly larger than that acting on the left side, leading to a large acceleration of the sphere directed from the bubble center to the sphere center. The bubble expands explosively afterwards (Fig.7 b) and the gas pressure decreases rapidly. The minimum pressure of the whole domain (around 0.2) is located around the bubble surface, which is much smaller than the hydrostatic pressure. Despite the sphere is moving leftwards at this moment, the hydrodynamic force acting on the sphere is directed rightward, thus decelerating the sphere. The left side of the bubble is flattened by the sphere when the bubble reaches the maximum volume, as shown in Fig.7 (c). Meanwhile, the sphere reaches the maximum displacement. In Fig.7 (a)-(c), the free surface has little effect on the bubble-sphere interaction , as suggested by the fact that the bubble is almost symmetric about the horizontal plane (*O*-*xy* plane).

During the bubble collapsing phase (Fig.7 d), the bubble top region collapses faster than other regions due to secondary Bjerknes force from the free surface while the presence of the sphere retards the motion of the left side of the bubble. Thereafter, the bubble top region becomes flattened and a local high pressure region is formed near the top right region of the bubble surface (Fig.7 e). This high pressure region further drives the collapse of the bubble top surface and finally leads to the formation of a downward jet (Fig.7 f), and the maximum dimensionless pressure of the high pressure region

increases to 30. Again, the pressure acting on the right side of the sphere is larger than that acting on the left side, leading to a large acceleration of the sphere directing leftward, i.e., the rightward velocity of the sphere decreases rapidly. In the numerical simulation, a very thin liquid jet originates on the left side of the bubble (Fig.7 f), and both the mesh density controller and mesh topology treatment are adopted to ensure the mesh to have quality therein; however, it's difficult to capture such detailed deformation features of the bubble in the present experiment due to the limited spatial resolution. As discussed above, overall qualitative agreement is achieved between numerical simulation and experimental observations.

In this and the subsequent sections, the times for experiment and simulation are not exactly the same, which can be explained as follows. In our experiments, bubbles are generated by the underwater electric discharge. The bubble contents may include vapor from water, vapor from the melted electrodes, plasma and so on [29, 52, 53]. It is quite difficult to model the detailed physical process at the stage of bubble inception. Following many publications [15, 29, 52, 54], the initial bubble in numerical simulations is set as a tiny high-pressure spherical bubble and the gas pressure during bubble oscillation is approximated by using the adiabatic law, which attributes to the slight difference of the bubble period between experiment and simulation.

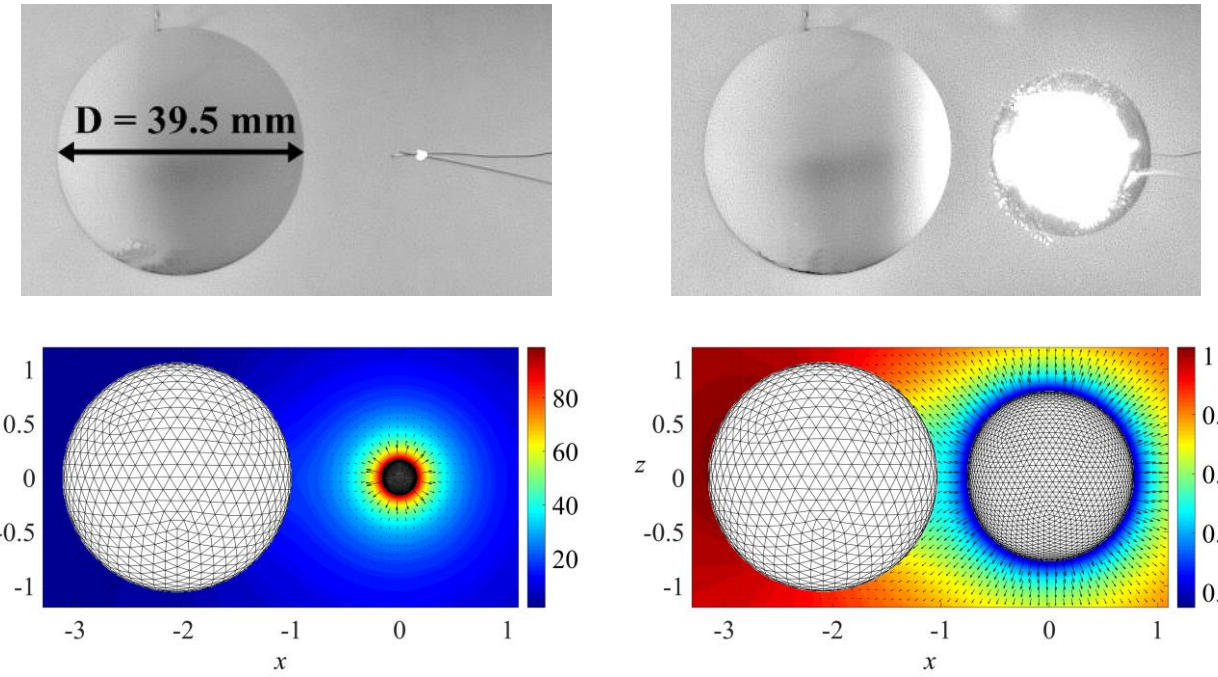

(a) $t_{exp} = 0$, $t_{num} = 2 \times 10^{-4}$ (b) $t_{exp} = 0.305$, $t_{num} = 0.301$

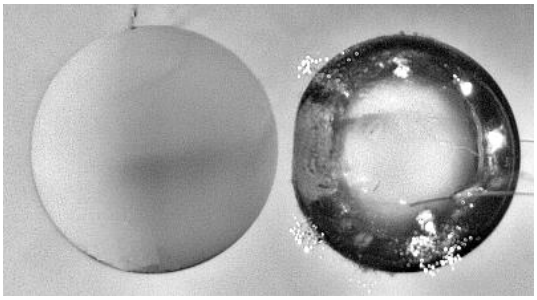

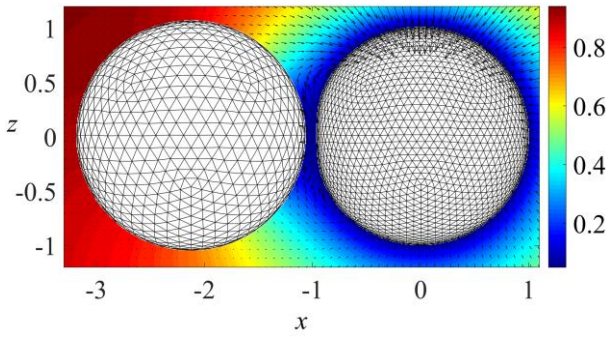

(c) t_{exp} = 0.916, t_{num} = 0.908

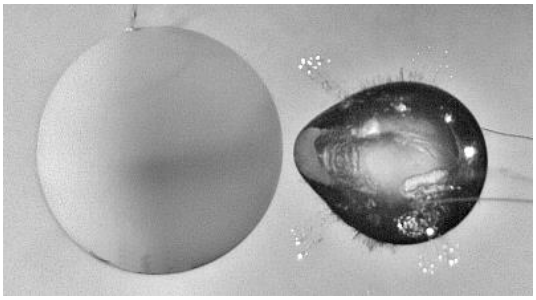

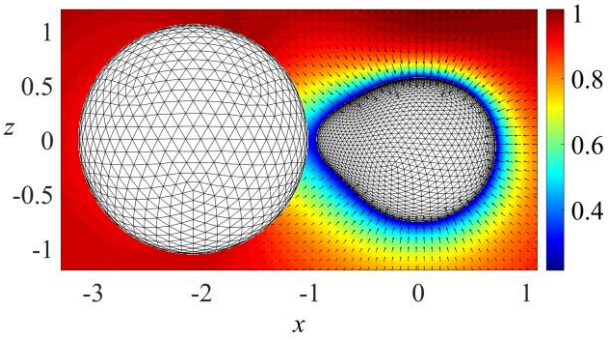

(d) t_{exp} = 1.503, t_{num} = 1.515

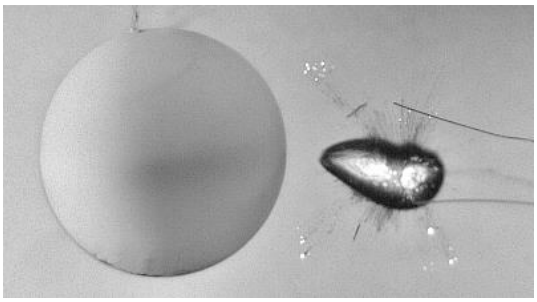

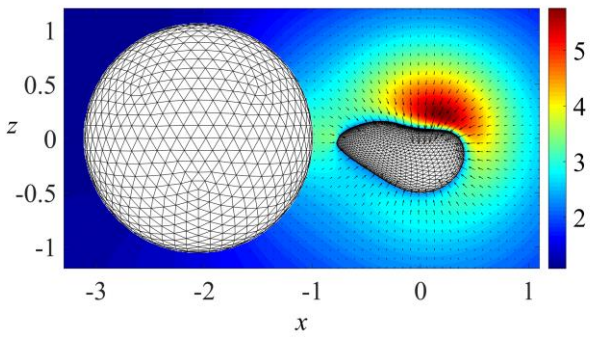

(e) t_{exp} = 1.691, t_{num} = 1.702

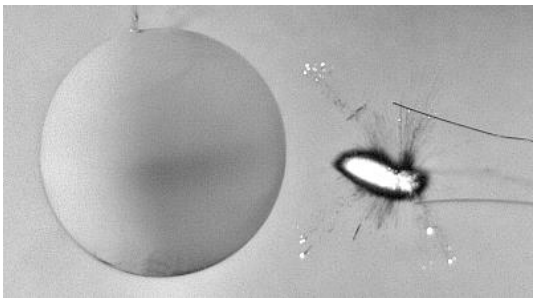

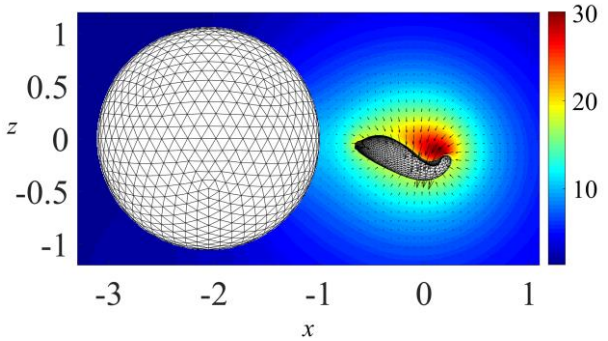

(f) t_{exp} = 1.715, t_{num} = 1.751

Fig. 7 Comparison of the bubble-sphere interaction beneath a free surface between experimental images and numerical simulations from FCM. The parameters in the experiment are: R_s = 19.75 mm, M = 32.3 g, R_m = 18.7 mm, h = 41.2 mm, (x_0, y_0, z_0) = (-38.5 mm, 0, 0). The dimensionless parameters adopted in the numerical computation are set as: λ_L = 1.06, λ_ρ = 1, $\left(\overline{x}_0, \overline{y}_0, \overline{z}_0\right)$ = (-2.05, 0, 0), γ_f = 2.2, ε = 100 and κ = 1.4.

Fig. 8 gives a quantitative comparison between the experimental data (red circles) and numerical results obtained by the FCM (blue solid line) and the LCM (green dashed line). The results obtained by both the methods correlate well with each other and with the experimental results during $t \in [0, 0.2]$, but then the discrepancy becomes more and more obvious. Nevertheless, an overall quantitative agreement is achieved between the numerical results and the experimental data, in terms of the sphere displacement. In this case, the sphere-bubble size ratio is larger than 1, thus the advantage of the FCM over the LCM is not fully displayed.

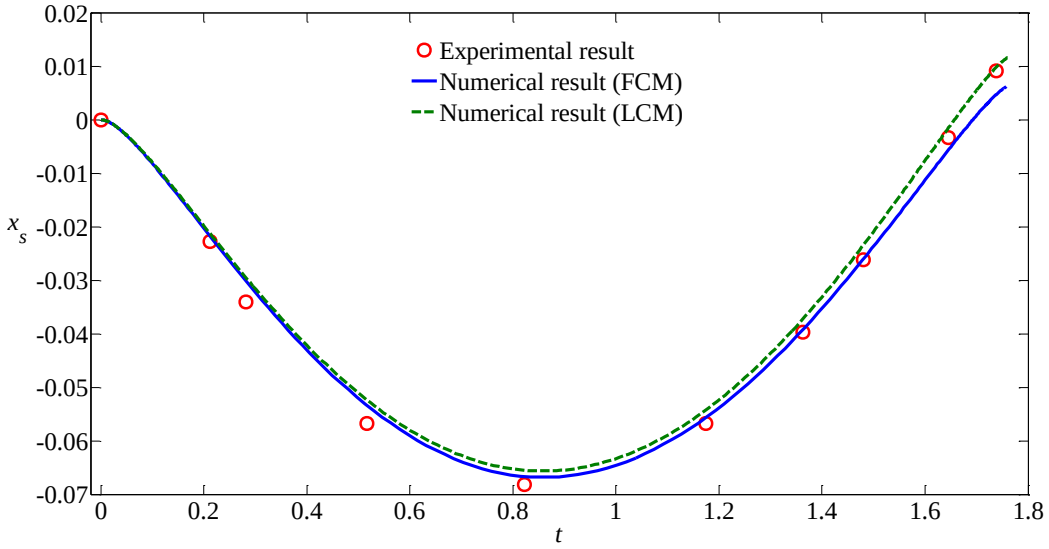

Fig. 8 Comparison of the dimensionless sphere displacement in the x axis direction between experiment (red circles), FCM (blue solid line) and LCM (green dashed line) for the same case in Fig. 7.

6.2 Bubble-sphere interaction near a rigid wall

The second experiment of bubble-sphere interaction is conducted near a vertical rigid wall. The parameters in the experiment are: M = 2.58 g, R_s = 8 mm, R_m = 15.6 mm, (x_0, y_0, z_0) = (20.5 mm, 0, 12.5 mm) and d_w = 21.0 mm. In addition, the initial bubble depth is about 200 mm, thus the effect of the free surface on the bubble-sphere interaction is ignored in this case. The initial parameters in the numerical simulation are set as: λ_L = 0.51, λ_ρ = 1.2, $\left(\overline{x}_0, \overline{y}_0, \overline{z}_0\right)$ = (1.31, 0, 0.8), γ_w = -1.34, ε = 100

and κ = 1.4. The Green function in Equation (4) is adopted to avoid the integrals over the rigid wall in the simulation, taken as:

$$G(\boldsymbol{r},\boldsymbol{q}) = \frac{1}{|\boldsymbol{r}-\boldsymbol{q}|} + \frac{1}{|\boldsymbol{r}-\boldsymbol{q}'|}, \tag{44}$$

where $\boldsymbol{q}'$ is the reflected image of $\boldsymbol{q}$ across the rigid wall.

Fig. 9 shows some selected images of the experiment and the corresponding numerical results, which illustrates the overall physical process during the first cycle of the bubble. Fig.9 (a)-(f) show the bubble-sphere interaction near a vertical wall at initiation, during expansion, at the maximum volume, during collapse, at the jet inception, and during the jet formation, respectively. The sphere is pushed upward and rightward during the bubble expansion phase (Fig.9 a-b). In Fig.9 (c), the bubble surface is slightly flattened by the rigid wall and the sphere simultaneously. Besides, the dimensionless pressure around the bubble surface decreases to less than 0.1, thus the bubble will be driven to collapse by the ambient hydrostatic pressure afterwards. In Fig.9 (d), a high curvature region is formed on the bubble surface due to the retardation effect of the sphere. As discussed above, the first jet (marked as A in Fig.9 e, denoted by 'jet A') originates on the highest-curvature region. Meanwhile, another jet (marked as B in Fig.9 e, denoted by 'jet B') is formed due to the secondary Bjerknes force from the rigid wall. In Fig.9 (f), the merge of the two jets is observed due to the close distance between the locations of jet A and jet B. However, the two jets develop in different directions, i.e., the liquids from different locations are rushing into a local region, leading to a splashing effect of the merged jet tip (marked as C in Fig.9 f) and maybe splitting of micro-droplets from the jet tip. In the 3D BIM simulation (FCM), although physical instabilities including the splitting of some micro-droplets are smoothed away by the present 'weighted least-square smoother', the essential physical features are well preserved.

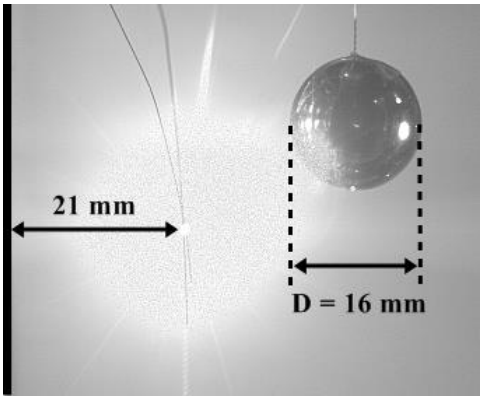

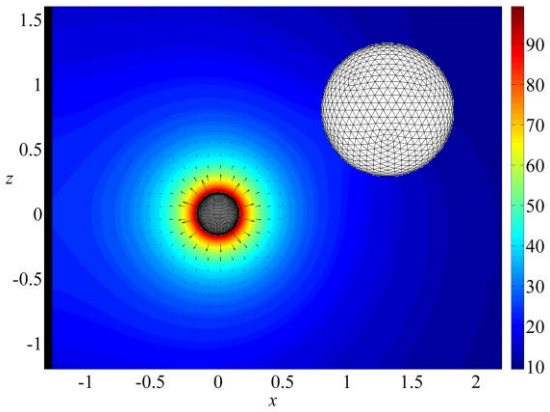

(a) $t_{exp} = 0$, $t_{num} = 2 \times 10^{-4}$

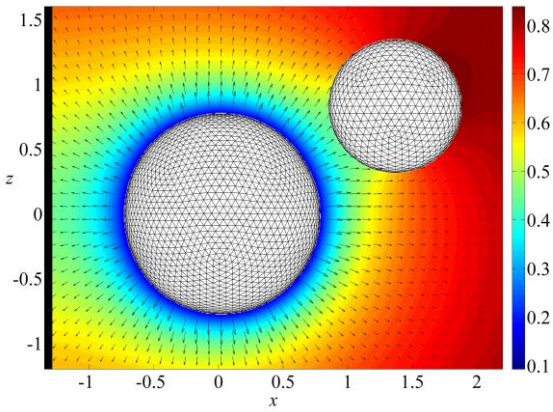

(b) $t_{exp} = 0.359$, $t_{num} = 0.342$

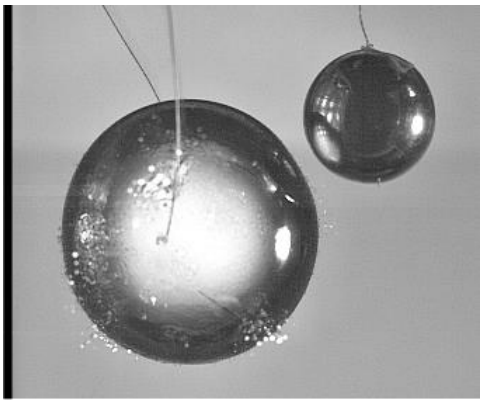

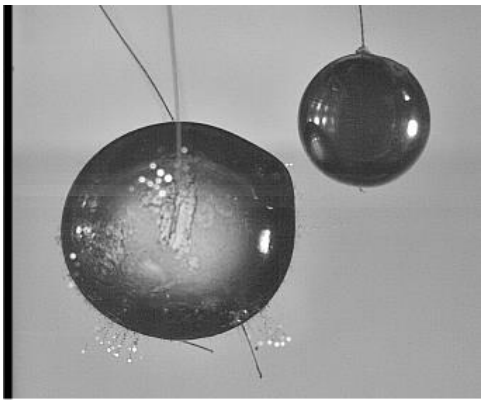

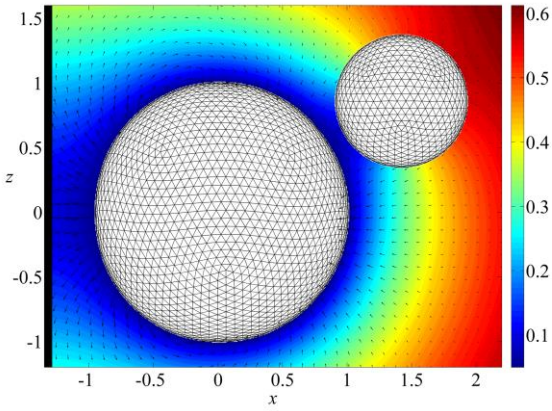

(c) $t_{exp} = 0$, $t_{num} = 1.065$

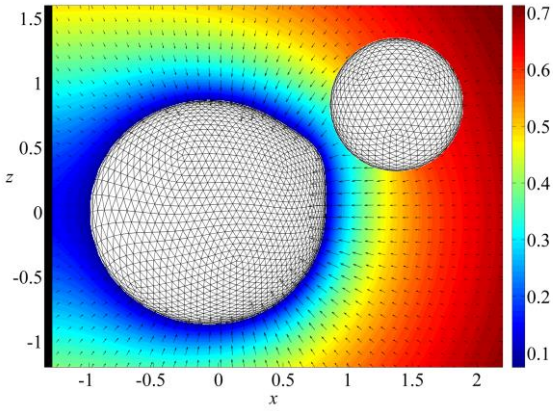

(d) $t_{exp} = 1.669$, $t_{num} = 1.646$

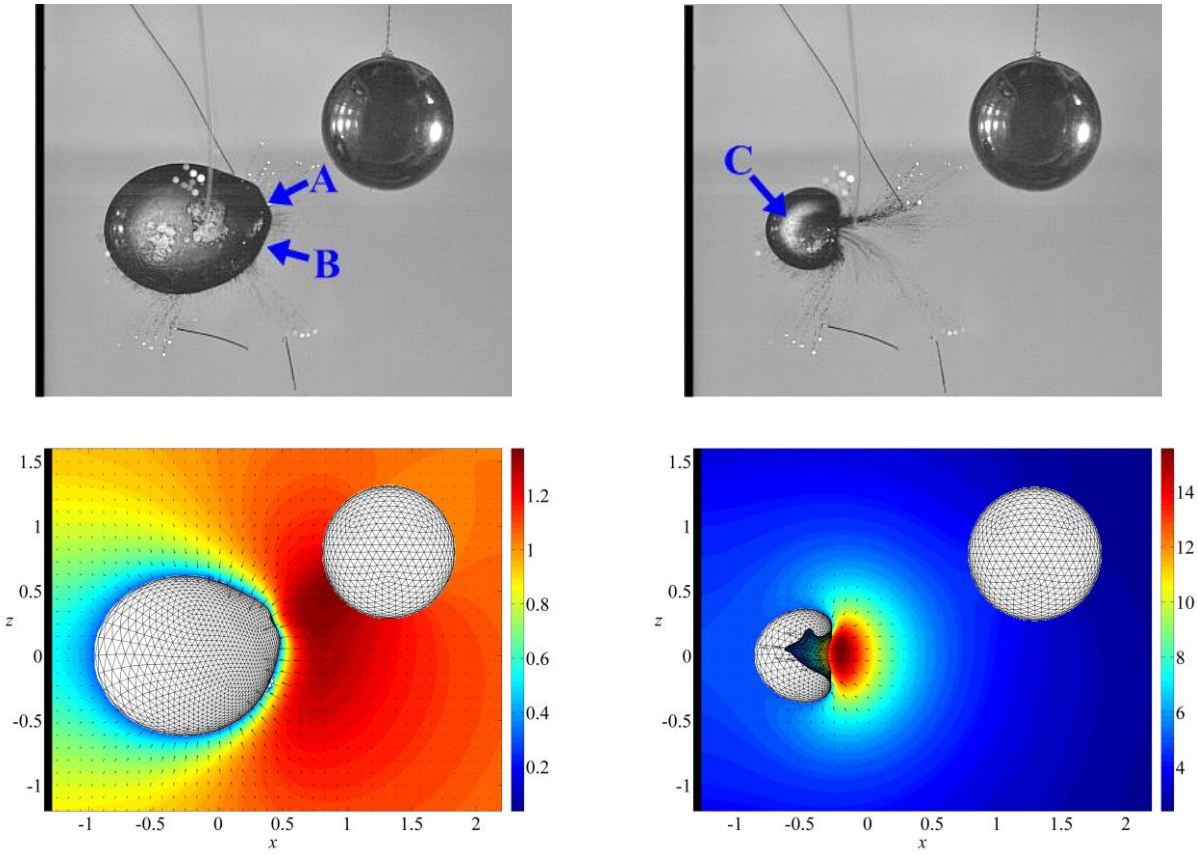

(e) t_{exp} = 2.001, t_{num} = 1.987 (f) t_{exp} =2.102, t_{num} = 2.181

Fig. 9 Comparison of the bubble-sphere interaction near a vertical rigid wall between experimental images and numerical simulations from FCM. The parameters in the experiment are: R_s = 8 mm, M = 2.58 g, R_m = 15.6 mm, (x_0, y_0, z_0) = (20.5 mm, 0, 12.5mm), d_w = 21.0 mm.. The dimensionless parameters adopted in the numerical computation are set as: $\lambda_L = 0.51$, $\lambda_\rho = 1.2$, $\left(\overline{x}_0, \overline{y}_0, \overline{z}_0\right)$ = (1.31, 0, 0.8), γ_w = -1.34, ε = 100 and κ = 1.4.

Fig. 10 shows a quantitative comparison between the experiment and numerical results obtained by the FCM and the LCM. The sphere displacement in x axis direction is shown in Fig.10 (a). It's worth noting that the result of the FCM agrees very well with the experimental data, while the maximum sphere displacement obtained by the LCM is significantly smaller than the experiment result. For the sphere displacement in z axis direction, similar results can be found. In this case, the FCM has higher accuracy than the LCM and the advantage of the FCM over the LCM is exhibited.

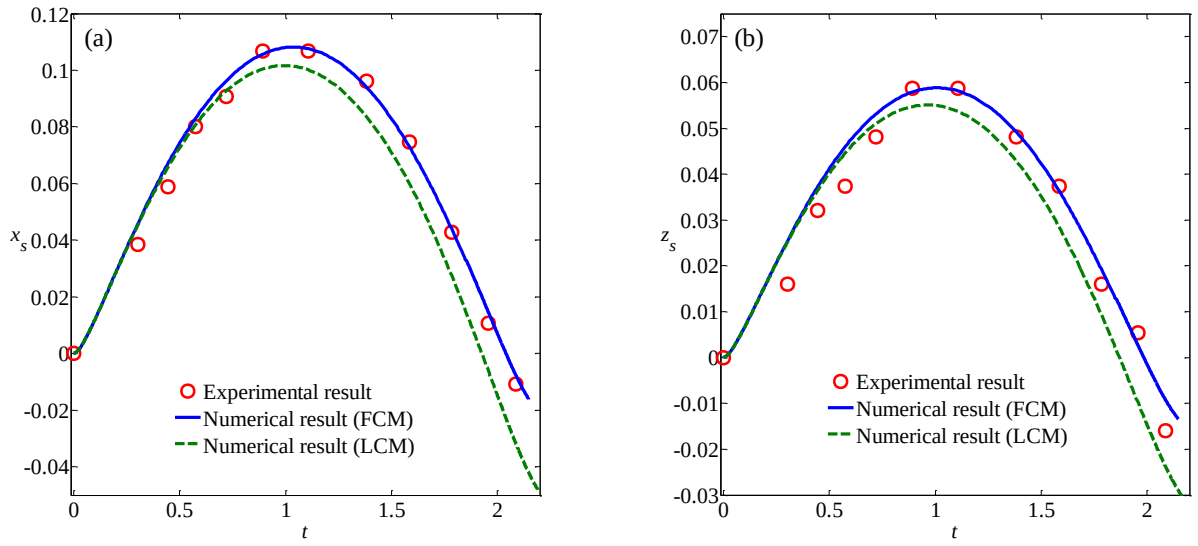

Fig. 10 Comparison of the sphere displacement in (a) x axis direction and (b) z axis direction between the results from experiment (red circles), FCM (blue solid line) and LCM (green dashed line) for the same case in Fig. 9.

6.3 Attached-bubble-sphere interaction

We further consider an interesting and challenging case, i.e., the interaction between a sphere and an attached-bubble near a vertical rigid wall. The parameters in the experiment are: M = 15.12 g, R_s = 16 mm, R_m = 18.5 mm, (x_0, y_0, z_0) = (0, 0, -16 mm) and d_w = 23.7 mm. The effect of the free surface is also ignored in this case. The initial parameters in the numerical simulation are set as: λ_L = 0.86, λ_ρ = 0.88, $\left(\overline{x}_0, \overline{y}_0, \overline{z}_0\right)$ = (0, 0, 0.86), γ_w = 1.28, ε = 37.35, $\overline{R}_0$ = 0.3 and κ = 1.4. The initial bubble center is placed on the top of the sphere in the experiment, thus the initial bubble shape cannot be treated as a sphere in this special case. Instead, we assume a nearly hemi-spherical bubble is attached to the sphere surface with a radius of R_0. We set $\overline{R}_0$ as 0.3 and adjust the strength parameter ε until $\overline{R}_m$ equals 1.

Fig. 11 shows the comparison between experimental observations and numerical results from FCM. During the early expansion phase of the bubble (Fig. 11 a), the pressure between the bubble and the rigid wall is enhanced, thus the bubble and sphere are slightly repelled by the rigid wall. When the bubble over-expands (Fig.11 b), the pressure between the bubble and the rigid wall is weakened, and

thus the bubble and sphere will be attracted towards the rigid wall. In Fig.11 (c), when the bubble reaches the maximum volume, the top part of the bubble is still expanding while the lower part of the bubble (the bubble-sphere intersection part) begins to collapse. An annular neck at the bubble-sphere intersection is observed in the experiment, and this important feature is well reproduced by the present numerical model. During the bubble collapsing phase, the annular neck further develops with an increase in the neck height, as shown in Fig.11 (d-e). Meanwhile, we note the great imbalance in the pressures on the left and right sides of the bubble, indicating that the bubble is pushed towards the rigid wall at this stage. In Fig.11 (e), an obvious asymmetric characteristic of the bubble shape is observed due to the faster collapse of the left side of the bubble. Thereafter, as shown in Fig.11 (f), the rightmost of the bubble surface is almost motionless under the retardation effect of the rigid wall while some liquid from the left side rushes into the neck and finally penetrates the top of the bubble surface (marked as A in Fig.11 f). The subsequent breakup of the bubble is beyond scope of this work.

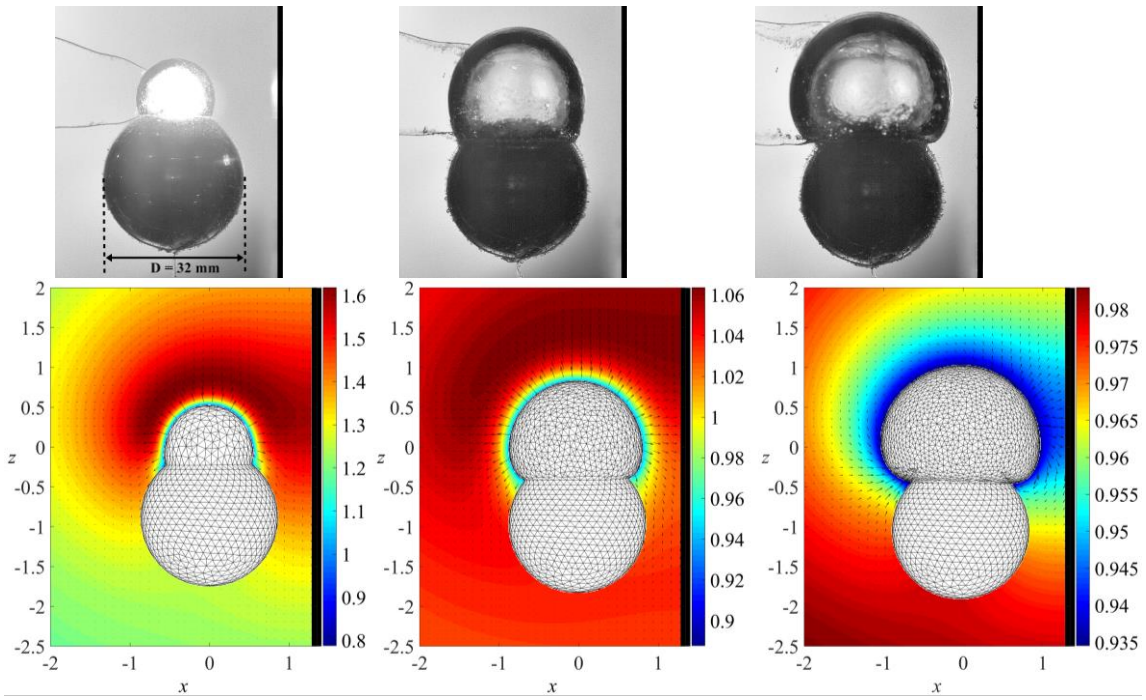

(a) t_{exp} = 0.122, t_{num} = 0.122 (b) t_{exp} = 0.426, t_{num} = 0.425 (c) t_{exp} = 1.005, t_{num} = 1.044

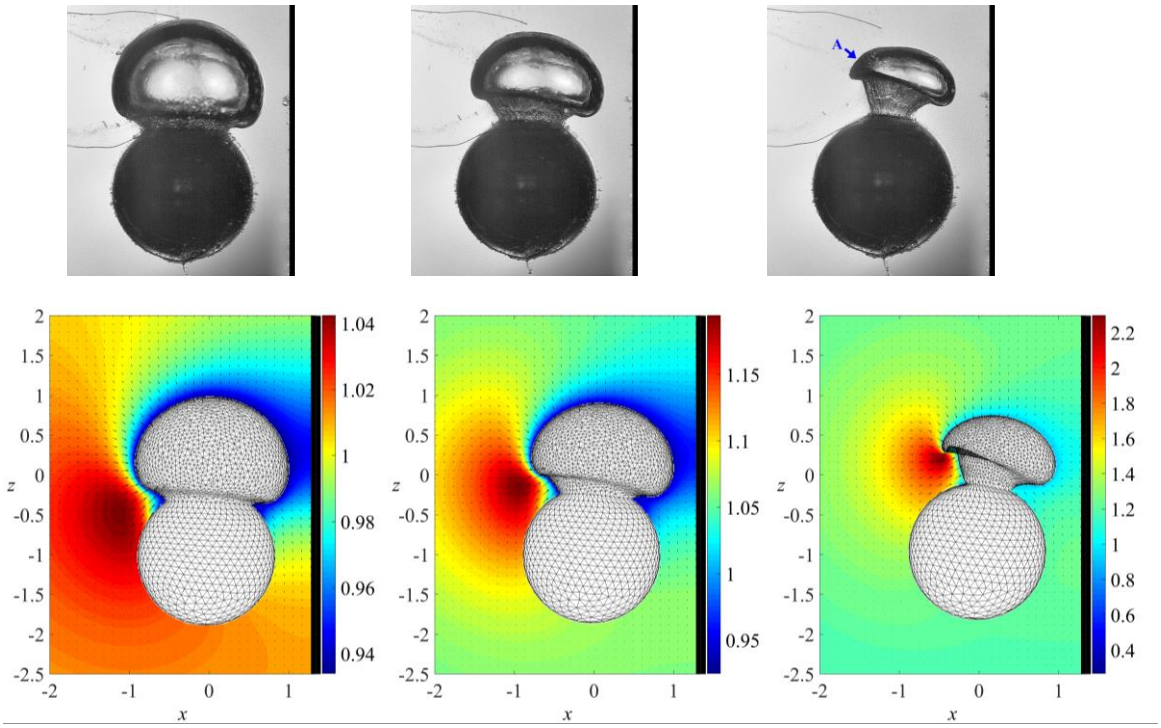

(d) t_{exp} = 1.462, t_{num} = 1.464 (e) t_{exp} = 1.675, t_{num} = 1.677 (f) t_{exp} = 1.828, t_{num} = 1.917

Fig. 11 Comparison of the attached-bubble-sphere interaction near a vertical wall between experimental images and numerical simulations from FCM. The parameters in the experiment are: R_s = 16 mm, M = 15.12 g, R_m = 18.5 mm, (x_0, y_0, z_0) = (0, 0, -16 mm) and d_w = 23.7 mm. The dimensionless parameters adopted in the numerical computation are set as: λ_L = 0.86, λ_ρ = 0.88, $\left(\overline{x}_0, \overline{y}_0, \overline{z}_0\right)$ = (0, 0, 0.86), γ_w = 1.28, ε = 37.35, $\overline{R}_0 = 0.3$ and κ = 1.4.

Fig. 12 shows a quantitative comparison of sphere displacement in the z axis direction between the experiment and numerical results obtained by the FCM and the LCM. Since the bubble is attached to the sphere surface, the FSI effect is extremely strong in this case and the maximum value of the sphere displacement reaches 0.2, which is several times that of the foregoing cases. Apparently, the numerical result obtained by the LCM is very different from the experimental result while the FCM gives the results that quite well agree with these of experiments, reflecting the distinct advantage of the FCM over the LCM.

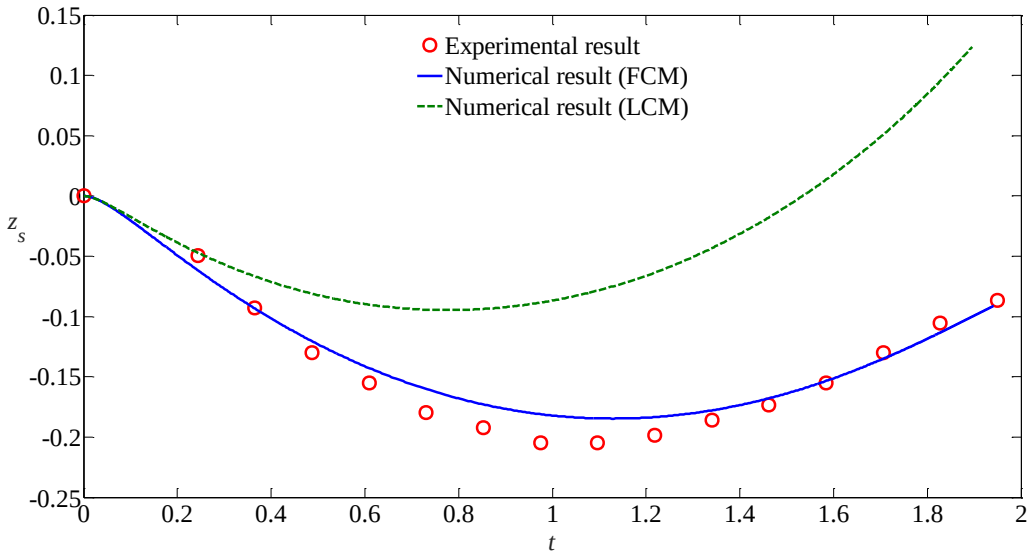

Fig. 12 Comparison of the sphere displacement in the z axis direction between experiment (red circles), FCM (blue solid line) and LCM (green dashed line) for the same case in Fig. 11.

7. Conclusions

Under the potential flow assumptions, a three-dimensional full coupling model (3D FCM) is established to simulate the transient pulsating-bubble-sphere interaction under various boundary conditions with particular focus on the dynamics of an attached bubble on the sphere surface. The FCM has complete theoretical basis as well as excellent performance in numerical simulations. In the present model, the auxiliary function method is used to deal with the mutual dependence between the hydrodynamic force and the sphere acceleration. Besides, several latest mesh optimization techniques are adopted to maintain a high quality of mesh on the surface. For a bubble attached on the sphere surface, the velocity at the three-phase contact line is calculated by the double-node technique, in which the bubble and the sphere boundary conditions are imposed on the contact line simultaneously. For axisymmetric-configuration case, the numerical results obtained by the present 3D FCM have extremely good agreement with those obtained by the axisymmetric model. Additionally, the pressure and velocity fields in 3D cases are calculated by the indirect boundary integral method, which help to reveal the underlying mechanisms of bubble dynamic behaviors.

Numerical results obtained by the traditional loose coupling model (LCM) and the present FCM

are compared in this study. It is noted that the accuracy of the LCM is greatly reduced in the following two situations: (i) the sphere-bubble size ratio λ_L decreases, especially when $\lambda_L < 1$; (ii) the sphere-liquid density ratio λ_ρ decreases, especially when $\lambda_\rho < 1$. Compared with the traditional LCM, the FCM maintains a higher accuracy and better stability.

At last, the present 3D FCM is proved to reproduces the experimental observations very well, including a challenging case in which the bubble is in contact with the sphere surface. The accuracy and robustness of the present model make it possible to be further extended to study more complex physical phenomena involved in underwater contact explosions, interaction between airgun-body and attached airgun-bubbles, etc.

Acknowledgements

This work is supported by the National Natural Science Foundation of China (51709056 and 11702071), the China Postdoctoral Science Foundation (2018T110276, 2017M620112 and 2017M621249) and the Heilongjiang Postdoctoral Fund (LBH-Z17049).

References

1. E. Klaseboer, K. C. Hung, C. Wang, C. W. Wang, B. C. Khoo, P. Boyce, S. Debono, andH. Charlier, "Experimental and numerical investigation of the dynamics of an underwater explosion bubble near a resilient/rigid structure," Journal of Fluid Mechanics **537**, 387 (2005).
2. J. X. Wang, Z. Zong, K. Liu, andJ. Cui, "Simulations of the dynamics and interaction between a floating structure and a near-field explosion bubble," Applied Ocean Research **78**, 50 (2018).
3. T. Li, S. Wang, S. Li, andA. M. Zhang, "Numerical investigation of an underwater explosion bubble based on FVM and VOF," Applied Ocean Research **74**, 49 (2018).
4. K. L. de Graaf, P. A. Brandner, andI. Penesis, "Bubble dynamics of a seismic airgun," Experimental Thermal and Fluid Science **55**, 228 (2014).
5. S. Zhang, S. P. Wang, A. M. Zhang, andP. Cui, "Numerical study on motion of the air-gun bubble based on boundary integral method," Ocean Engineering **154**, 70 (2018).
6. C. E. Brennen, *Cavitation and bubble dynamics* (Cambridge University Press, 1995).
7. X. Long, H. Cheng, B. Ji, R. E. A. Arndt, andX. Peng, "Large eddy simulation and Euler–Lagrangian coupling investigation of the transient cavitating turbulent flow around a twisted hydrofoil," International Journal of Multiphase Flow **100**, 41 (2018).
8. O. Supponen, D. Obreschkow, P. Kobel, M. Tinguely, N. Dorsaz, andM. Farhat, "Shock waves from nonspherical cavitation bubbles," Physical Review Fluids **2**, 093601 (2017).
9. G. L. Chahine, A. Kapahi, J. K. Choi, andC. T. Hsiao, "Modeling of surface cleaning by cavitation bubble dynamics and collapse," Ultrasonics Sonochemistry **29**, 528 (2016).

10. F. Reuter, andR. Mettin, "Mechanisms of single bubble cleaning," Ultrasonics Sonochemistry **29**, 550 (2016).
11. J. E. Lingeman, J. A. McAteer, E. Gnessin, andA. P. Evan, "Shock wave lithotripsy: advances in technology and technique," Nature Reviews Urology **6**, 660 (2009).
12. C.-D. Ohl, M. Arora, R. Ikink, N. De Jong, M. Versluis, M. Delius, andD. Lohse, "Sonoporation from jetting cavitation bubbles," Biophysical journal **91**, 4285 (2006).
13. P. Cui, A. M. Zhang, andS. P. Wang, "Small-charge underwater explosion bubble experiments under various boundary conditions," Physics of Fluids **28**, 117103 (2016).
14. E. Cox, A. Pearson, J. R. Blake, andS. R. Otto, "Comparison of methods for modelling the behaviour of bubbles produced by marine seismic airguns," Geophysical prospecting **52**, 451 (2004).
15. E. A. Brujan, G. S. Keen, A. Vogel, andJ. R. Blake, "The final stage of the collapse of a cavitation bubble close to a rigid boundary," Physics of Fluids **14**, 85 (2002).
16. O. Supponen, D. Obreschkow, M. Tinguely, P. Kobel, N. Dorsaz, andM. Farhat, "Scaling laws for jets of single cavitation bubbles," Journal of Fluid Mechanics **802**, 263 (2016).
17. J. R. Blake, M. C. Hooton, P. B. Robinson, andR. P. Tong, "Collapsing cavities, toroidal bubbles and jet impact," Philosophical Transactions of the Royal Society of London A: Mathematical, Physical and Engineering Sciences **355**, 537 (1997).
18. X. Huang, Q.-X. Wang, A. M. Zhang, andJ. Su, "Dynamic behaviour of a two-microbubble system under ultrasonic wave excitation," Ultrasonics Sonochemistry **43**, 166 (2018).
19. J. R. Blake, andD. Gibson, "Cavitation bubbles near boundaries," Annual Review of Fluid Mechanics **19**, 99 (1987).
20. S. Zhang, J. H. Duncan, andG. L. Chahine, "The final stage of the collapse of a cavitation bubble near a rigid wall," Journal of Fluid Mechanics **257**, 147 (1993).
21. A. M. Zhang, S. Li, andJ. Cui, "Study on splitting of a toroidal bubble near a rigid boundary," Physics of Fluids **27**, 062102 (2015).
22. Y. L. Zhang, K. S. Yeo, B. C. Khoo, andC. Wang, "3D Jet Impact and Toroidal Bubbles," Journal of Computational Physics **166**, 336 (2001).
23. C. Wang, andB. C. Khoo, "An indirect boundary element method for three-dimensional explosion bubbles," Journal of Computational Physics **194**, 451 (2004).
24. A. M. Zhang, andY. L. Liu, "Improved three-dimensional bubble dynamics model based on boundary element method," Journal of Computational Physics **294**, 208 (2015).
25. J. R. Blake, B. B. Taib, andG. Doherty, "Transient cavities near boundaries. Part 1. Rigid boundary," Journal of Fluid Mechanics **170**, 479 (1986).
26. J. Best, "The formation of toroidal bubbles upon the collapse of transient cavities," Journal of Fluid Mechanics **251**, 79 (1993).
27. E. Klaseboer, B. C. Khoo, andK. C. Hung, "Dynamics of an oscillating bubble near a floating structure," Journal of Fluids and Structures **21**, 395 (2005).
28. P. Harris, "A numerical method for predicting the motion of a bubble close to a moving rigid structure," Communications in Numerical Methods in Engineering **9**, 81 (1993).
29. G. L. Chahine, K. M. Kalumuck, andC. T. Hsiao, "Simulation of surface piercing body coupled response to underwater bubble dynamics utilizing 3DYNAFS, a three-dimensional BEM code," Computational Mechanics **32**, 319 (2003).
30. Z. R. Li, L. Sun, andZ. Zong, "Numerical analysis of gas bubbles in close proximity to a movable or deformable body," Archive of Applied Mechanics **83**, 1715 (2013).

31. B. M. Borkent, M. Arora, C. D. Ohl, N. De Jong, M. Versluis, D. Lohse, K. A. MØrch, E. Klaseboer, andB. C. Khoo, "The acceleration of solid particles subjected to cavitation nucleation," Journal of Fluid Mechanics **610**, 157 (2008).
32. J. H. Duncan, C. D. Milligan, andS. Zhang, "On the interaction between a bubble and a submerged compliant structure," Journal of Sound and Vibration **197**, 17 (1996).
33. K. M. Kalumuck, R. Duraiswami, andG. L. Chahine, "Bubble dynamics fluid-structure interaction simulation by coupling fluid BEM and structural FEM codes," Journal of Fluids and Structures **9**, 861 (1995).
34. M. Dawoodian, A. Dadvand, andA. Nematollahi, "Simulation of bubble dynamics near a plate with an aperture in a vertical cylinder using a combined boundary element-finite difference method," Engineering Analysis with Boundary Elements **59**, 187 (2015).
35. Z. Zong, J. X. Wang, L. Zhou, andG. Y. Zhang, "Fully nonlinear 3D interaction of bubble dynamics and a submerged or floating structure," Applied Ocean Research **53**, 236 (2015).
36. S. Li, R. Han, andA. M. Zhang, "Nonlinear interaction between a gas bubble and a suspended sphere," Journal of Fluids and Structures **65**, 333 (2016).
37. B. Y. Ni, A. M. Zhang, andG. X. Wu, "Numerical and experimental study of bubble impact on a solid wall," Journal of Fluids Engineering **137**, 031206 (2015).
38. S. Li, A. M. Zhang, R. Han, andY. Q. Liu, "Experimental and numerical study on bubble-sphere interaction near a rigid wall," Physics of Fluids **29**, 092102 (2017).
39. S. Wu, Z. Zuo, H. A. Stone, andS. Liu, "Motion of a Free-Settling Spherical Particle Driven by a Laser-Induced Bubble," Physical Review Letters **119**, 084501 (2017).
40. Y. Zhang, Y. Zhang, Z. Qian, B. Ji, andY. Wu, "A review of microscopic interactions between cavitation bubbles and particles in silt-laden flow," Renewable and Sustainable Energy Reviews **56**, 303 (2016).
41. Y. Zhang, F. Chen, Y. Zhang, Y. Zhang, andX. Du, "Experimental investigations of interactions between a laser-induced cavitation bubble and a spherical particle," Experimental Thermal and Fluid Science (2018).
42. S. Li, R. Han, A. M. Zhang, andQ. X. Wang, "Analysis of pressure field generated by a collapsing bubble," Ocean Engineering **117**, 22 (2016).
43. S. Rungsiyaphornrat, E. Klaseboer, B. C. Khoo, andK. S. Yeo, "The merging of two gaseous bubbles with an application to underwater explosions," Computers & Fluids **32**, 1049 (2003).
44. T. T. Bui, E. T. Ong, B. C. Khoo, E. Klaseboer, andK. C. Hung, "A fast algorithm for modeling multiple bubbles dynamics," Journal of Computational Physics **216**, 430 (2006).
45. C. Wang, B. C. Khoo, andK. S. Yeo, "Elastic mesh technique for 3D BIM simulation with an application to underwater explosion bubble dynamics," Computers & Fluids **32**, 1195 (2003).
46. Q. X. Wang, "The evolution of a gas bubble near an inclined wall," Theoretical and computational fluid dynamics **12**, 29 (1998).
47. Y. L. Liu, S. P. Wang, andA. M. Zhang, "Interaction between bubble and air-backed plate with circular hole," Physics of Fluids **28**, 062105 (2016).
48. J. Duncan, andS. Zhang, "On the interaction of a collapsing cavity and a compliant wall," Journal of Fluid Mechanics **226**, 401 (1991).
49. Q. X. Wang, "Unstructured MEL modelling of nonlinear unsteady ship waves," Journal of Computational Physics **210**, 368 (2005).
50. R. Han, S. Li, A. M. Zhang, andQ. X. Wang, "Modelling for three dimensional coalescence of two

bubbles," Physics of Fluids **28**, 062104 (2016).
51. W. Lauterborn, "Cavitation bubble dynamics—new tools for an intricate problem," Applied Scientific Research **38**, 165 (1982).
52. B. H. T. Goh, S. W. Gong, S.-W. Ohl, andB. C. Khoo, "Spark-generated bubble near an elastic sphere," International Journal of Multiphase Flow **90**, 156 (2017).
53. T. Sato, M. Tinguely, M. Oizumi, andM. Farhat, "Evidence for hydrogen generation in laser-or spark-induced cavitation bubbles," Applied Physics Letters **102**, 074105 (2013).
54. S. W. Gong, S. W. Ohl, E. Klaseboer, andB. C. Khoo, "Interaction of a spark-generated bubble with a two-layered composite beam," Journal of Fluids and Structures **76**, 336 (2018).